AIMS Mathematics, 11(1): 3096–3131.
DOI: 10.3934/math.2026123
Received: 22 November 2025
Revised: 11 January 2026
Accepted: 16 January 2026
Published: 30 January 2026

https://www.aimspress.com/journal/Math

Research article

Dynamics of the generalized derivative resonant NLS equation: bifurcation, exact solutions, and the transition from periodic to chaotic waves

Adel Emandouh*

Department of Mathematics and Statistics, College of Science, King Faisal University, P. O. Box 400, Al-Ahsa 31982, Saudi Arabia

* **Correspondence:** aelmandouh@kfu.edu.sa.

Abstract: This work presents a inclusive inspection of the nonlinear dynamics of the generalized derivative resonant nonlinear Schrödinger equation (GD-RNLS), a fundamental model for wave phenomena in dispersive media. We use a tailored transformation to recast the GD-RNLS as a two-dimensional conservative dynamic system, which is equivalent to a Hamiltonian system with a single degree of freedom. Leveraging the Hamiltonian framework, we perform a detailed bifurcation analysis. The corresponding phase portraits are constructed, and we studied the degeneracy of the phase plane trajectories as the bifurcation parameter varies. Within this dynamic systems approach, we derive a family of novel exact solutions, categorizing them as periodic, super-periodic, kink (and anti- kink), and solitary wave solutions; selected solutions are illustrated graphically to clarify their properties. Furthermore, we examine a perturbed variant of the GD-RNLS, incorporating an external periodic forcing term modeled by a Jacobi elliptic function. The influence of this perturbation is explored numerically through two-dimensional (2D) and three- dimensional (3D) phase portraits, as well as the time series. Our simulations reveal a sequence of behavioral transitions: the system's initially periodic state gives way to quasi-periodic dynamics as the forcing frequency increases. Upon a further increase in frequency, chaotic behavior emerges. This transition to chaos is quantitatively confirmed by calculating the largest Lyapunov exponent and qualitatively visualized by the irregular structure of the Poincaré surface of section, both of which underscore the complex, stochastic nature of the system's dynamics under strong forcing.

Keywords: Shrödinger equation; bifurcation theory; wave solutions; quasi-periodic; chaotic pattern
Mathematics Subject Classification: 34H10, 35B20, 35C05, 35C075

1. Introduction

Nonlinear partial differential equations (NPDEs) are a vital branch of modern mathematics, playing a crucial role across various disciplines, including optics [1, 2], biology [3], and fluid dynamics [4,5]. Consequently, developing accurate analytical or approximate solutions for NPDEs has become essential. These solutions offer deep insights into the underlying physical models, allowing researchers to predict the evolution of real-world physical states and to validate the accuracy of numerical simulations. Finding these explicit analytical expressions—whether in the form of finite or infinite series—or obtaining physically significant special solutions (such as solitary waves, traveling waves, elliptic functions, or periodic waves) [6–8] is considered to be the most effective approach. This is because such exact solutions not only provide a robust foundation for qualitative research but also serve as a benchmark for assessing the quality and reliability of numerical methods. Recent developments in both analytical frameworks and computational methodologies have significantly improved the precision with which physical systems governed by NPDEs are examined. The quest for exact solutions increasingly draws upon advanced mathematical tools capable of navigating the intricacies of nonlinear behavior. Progress in partial differential equation (PDE) theory continues to expand the scope of solvable models, offering deeper insight into complex dynamics. Importantly, the interplay between rigorous analysis and numerical experimentation remains a cornerstone of contemporary research, driving innovation and refinement across diverse scientific domains. A wide array of advanced techniques has been devised by the scientific community to tackle such equations, with several methods emerging as particularly influential in recent studies. These include the classical Lie symmetry technique [9] and the bifurcation theory [11, 14].

The soliton propagation dynamics in nonlinear optical media are fundamentally governed by the nonlinear Schrödinger (NLS) equation [16, 17], which encapsulates the interplay between dispersion and nonlinear effects that shape the evolution of optical pulses. The NLS equation thus serves as a cornerstone for understanding soliton phenomena in diverse optical settings. For instance, Wazwaz and Mehanna [18] investigated the generation of both dark and bright solitons within a $(3+1)$-dimensional framework, offering insights into solitons' formation and propagation in higher-dimensional optical media. In a related study, Triki et al. [19] examined optical solitons under quadratic–cubic nonlinearity and derived associated conservation laws—key tools for assessing solitons' stability and dynamic behavior. Furthermore, Zhou et al. [20] presented exact optical solutions in metamaterials characterized by cubic–quintic nonlinearity and third-order dispersion. Their findings underscore the potential of metamaterials to enable novel mechanisms for manipulating soliton dynamics, owing to their engineered electromagnetic properties.

The present study aims to conduct a qualitative analysis of the following GD-RNLS equation [21]:

$$i\frac{\partial\phi}{\partial t} + a_1\frac{\partial^2\phi}{\partial x^2} + a_2(|\phi|^2\phi) + a_3(|\phi|^4\phi) + a_4\left(\frac{\frac{\partial^2|\phi|}{\partial x^2}}{|\phi|}\right)\phi + ia_5\frac{\partial}{\partial x}\left(|\phi|^2\phi\right) = 0, \tag{1.1}$$

where $\phi = \phi(x,t)$ denotes the complex-valued wave profile, which is dependent on the spatial coordinate x and time t. This function characterizes both the amplitude of the wave at a given time and its spatial distribution along the x-axis. Equation (1.1) comprises several terms, each reflecting distinct physical effects. The first term captures the system's temporal evolution. The group velocity dispersion is described by the second term, scaled by the coefficient a_1. The cubic nonlinearity is detected by the

third term characterized by the constant a_2, while quintic nonlinearity is specified by the fourth term characterized by the constant a_3. The fifth term, associated with the coefficient a_4, models' resonance effects—often interpreted as the quantum or Bohm potential. Finally, the self-steepening behavior in derivative form is described by the last term and is characterized by the coefficient a_5.

The GD-RNLS equation is an extension of the classical NLS equation, distinguished by the inclusion of higher-order spatial derivatives [22–24]. This generalized model is a cornerstone in nonlinear optics, where it is extensively used to simulate light propagation in various nonlinear media. It is particularly valuable for analyzing complex phenomena such as four-wave mixing, the formation of optical solitons, and modulation instability. The GD-RNLS equation has been the subject of numerous investigations. For example, Das et al. [25] performed a modulation stability analysis and examined the structure of optical chirped solitons. In a subsequent effort, the same authors [21] successfully derived periodic and solitary wave solutions for the GD-RNLS equation incorporating cubic–quintic nonlinearity. Separately, Behera [26] explored the quadratic resonance and the dynamical solutions within a perturbed NLS equation. Furthermore, the authors of [27] utilized a novel generalized exponential rational function method to obtain exact special solutions. More recently, the authors of [28] introduced a variety of physical solution structures for a generalized resonant dispersive NLS equation featuring power-law nonlinearity.

We note that to the best of our knowledge, a comprehensive qualitative analysis of Eq (1.1) has not yet been presented in the existing literature. This gap motivates the present study, which aims to enrich the theoretical framework by investigating the nonlinear dynamics of the system. Specifically, we perform a bifurcation analysis, construct phase portraits, and explore quasi- periodic and chaotic patterns. In addition, we derive new exact solutions to further illuminate the underlying wave phenomena.

This paper is arranged in the subsequent manner: Section 2 presents the reduction of the GD-RNLS equation to a two-dimensional (2D) dynamic system via a suitable transformation, followed by bifurcation analysis and phase portrait investigation. Section 3 outlines the procedures for constructing new exact solutions to the GD-RNLS equation. Section 4 provides 2D and 3D graphical representations of selected solutions. Section 5 explores the influence of external periodic perturbations on the dynamic behavior of Eq (1.1). Section 6 provides a summary of the key findings of this study.

2. Bifurcation analysis

This section aims to study the bifurcations of the solution to Eq (1.1). We postulate that Eq (1.1) has a solution in the form

$$\phi(x,t) = \psi(\zeta)\exp[i(\alpha t - \beta x) + i\mu(\zeta)], \quad \zeta = x - \varpi t, \tag{2.1}$$

where $\psi(\zeta)$ and $\mu(\zeta)$ represent real-valued functions, while ϖ denotes the transverse velocity. Furthermore, the parameters β and α correspond to the spatial propagation constant and the temporal frequency shift, respectively. By substituting Eq (2.1) into Eq (1.1) and separating the resulting expression into its real and imaginary components, we obtain the following

Real part:

$$(a_1 + a_2)\psi'' - a_1\psi\mu'^2 + [(\varpi + 2a_1\beta)\psi - a_5\psi^3]\mu' + a_3\psi^5 + a_5\beta\psi^3 + s_2\psi^3 - (a_1\beta^2 + \alpha)\psi = 0. \tag{2.2}$$

Imaginary part:

$$3a_5\psi^2\psi' + a_1\psi\mu'' + 2a_1\psi'\mu' - (2a_1\beta + \varpi)\psi' = 0, \tag{2.3}$$

where the primes indicate differentiation with respect to ζ. Multiplying Eq (2.3) by ψ, we obtain

$$3a_5\psi^3\psi' + a_1\psi^2\mu'' + 2a_1\psi\psi'\mu' - (2a_1\beta + \varpi)\psi\psi' = 0. \tag{2.4}$$

Taking $(\psi^2\mu')' = \psi^2\mu'' + 2\psi\psi'\mu'$ into account, Eq (2.4) reduces to

$$3a_5\psi^3\psi' + a_1(\psi^2\mu')' - (2a_1\beta + \varpi)\psi\psi' = 0. \tag{2.5}$$

Integrating Eq (2.5) with respect to ζ and setting the integration constant to zero yields

$$\frac{3}{4}a_5\psi^4 + a_1\psi^2\mu' - \frac{1}{2}(2a_1\beta + \varpi)\psi^2 = 0. \tag{2.6}$$

Solving Eq (2.6) for μ' gives

$$\mu' = \frac{1}{4a_1}[2\varpi + 4a_1\beta - 3a_5\psi^2]. \tag{2.7}$$

Integrating the last equation then provides

$$\mu(\zeta) = \frac{\varpi + 2a_1\beta}{2a_1}\zeta - \frac{3a_5}{4a_1}\int \psi^2(\xi)\mathrm{d}\zeta. \tag{2.8}$$

Inserting Eq (2.8) into Eq (2.2), we obtain

$$\psi'' - p\psi - q\psi^3 - r\psi^5 = 0, \tag{2.9}$$

where p, q, and r are constants introduced for simplicity and they are given by

$$p = -\frac{\varpi^2 + 4a_1(\beta\varpi - \alpha)}{4a_1(a_1 + a_4)}, \quad q = -\frac{2a_1a_2 - a_5\varpi}{2a_1(a_1 + a_4)}, \quad r = -\frac{16a_1a_3 + 3a_5^2}{16a_1(a_1 + a_4)}. \tag{2.10}$$

Thus, the problem of finding the solution (2.1) to Eq (1.1) is reduced to finding $\psi(\zeta)$, which is a solution to Eq (2.9). Therefore, the range of the parameters p, q, and r must be selected carefully. One of the best methods for determining this range is bifurcation analysis. In [29], the authors systematically develop bifurcation theory as a tool for analyzing the qualitative behavior of dynamic systems, particularly how the equilibria and phase portraits change with the parameters. The core idea is to classify solution regimes—such as the number and stability of equilibrium points—based on parameter constraint.

By defining $\psi(\zeta) = R(\zeta)$, Eq (2.9) can be written as a two-dimensional dynamic system of the form:

$$\begin{cases} \psi' = R, \\ R' = -\psi(p + q\psi^2 + r\psi^4). \end{cases} \tag{2.11}$$

The system (2.11) is conservative because $\mathrm{div}(\psi', R') = \frac{\partial\psi'}{\partial\psi} + \frac{\partial R'}{\partial R} = 0$. The system (2.11) is Hamiltonian if it can be derived from a Hamiltonin function $\mathcal{H}(\psi, R)$ using Hamilton canonical equations [30], i.e.,

$$\psi' = \frac{\partial\mathcal{H}}{\partial R}, \quad R' = -\frac{\partial\mathcal{H}}{\partial\psi}. \tag{2.12}$$

By comparing both Eqs (2.11) and (2.12), we obtain

$$\frac{\partial \mathcal{H}}{\partial R} = R, \quad \frac{\partial \mathcal{H}}{\partial \psi} = \psi(p + q\psi^2 + r\psi^2). \tag{2.13}$$

We solve Eq (2.13) to get the Hamiltonian function $\mathcal{H}$. Hence, we have

$$\begin{aligned} \mathrm{d}\mathcal{H} &= \frac{\partial \mathcal{H}}{\partial R}\mathrm{d}R + \frac{\partial \mathcal{H}}{\partial \psi}\mathrm{d}\psi, \\ &= R\mathrm{d}R + \psi(p + q\psi^2 + r\psi^2)\mathrm{d}\psi. \end{aligned} \tag{2.14}$$

Thus, the integration of Eq (2.14) yields the Hamilton function $\mathcal{H}$ in the form

$$\mathcal{H} = \frac{1}{2}R^2 + V(\psi), \tag{2.15}$$

with the potential function $V(\psi)$ defined as

$$V(\psi) = \frac{p}{2}\psi^2 + \frac{q}{4}\psi^4 + \frac{r}{6}\psi^6. \tag{2.16}$$

The integration constant arises as an additive term in the potential function (2.16) and can be ignored without loss of generality, as it does not influence the dynamics. This follows from the fact that the Hamiltonian equations are generated by derivatives of the Hamiltonian $\mathcal{H}$, rendering such additive constants irrelevant. The condition $\partial_\zeta \mathcal{H} = 0$ implies that the Hamiltonian is a conserved quantity [31]. Therefore, it remains constant along any phase orbit, leading to the relation

$$\frac{1}{2}R^2 + \frac{p}{2}\psi^2 + \frac{q}{4}\psi^4 + \frac{r}{6}\psi^6 = \nu, \tag{2.17}$$

where ν is the constant value of $\mathcal{H}$ on a given orbit. The Hamiltonian (2.15) therefore provides a physical description of the motion of a unit-mass particle under the influence of the three-parameter potential (2.16). The conserved quantity (2.17) clearly consists of two terms: The first corresponds to the kinetic energy of a unit-mass particle, while the second coincides with the potential function (2.16). As a result, it has the standard mechanical interpretation of conserved total energy. Consequently, solving Eq (1.1) is equivalent to determining the trajectory of this particle. The relevance of this equivalence will be discussed later.

We now use this Hamiltonian framework to analyze the bifurcation behavior of system (2.11). The following theorem underpins this analysis.

Theorem 1. *(Lagrange theorem) [32] In conservative systems, stable equilibrium points occur precisely at the positions where the potential energy reaches a strict minimum.*

According to Lagrange's theorem, the equilibrium configurations are identified as the critical points of the potential function (2.16). Their qualitative nature—whether they represent a center (minimum) or a saddle (maximum)—is determined by the type of extremum of $V(\psi)$. For further clarification, see Appendix.

The equilibrium points take the form $(\psi_e, 0)$, where ψ_e satisfies the nonlinear algebraic equation

$$\psi_e(p + q\psi_e^2 + r\psi_e^4) = 0. \tag{2.18}$$

It is obvious that Eq (2.18) is symmetric about the origin. Consequently, all equilibrium points lie on the ψ- axis and are symmetrically distributed. The number of equilibrium points in the system (2.11) relies on the specific values of p, q, and r, which determine the real solutions of Eq (2.18). Clearly, the origin $O = (0, 0)$ is always an equilibrium point, while the remaining equilibria are obtained from

$$p + q\wp + r\wp^2 = 0, \qquad \wp = \psi_e^2. \tag{2.19}$$

Since $\wp = \psi_e^2 \geq 0$, the roots of Eq (2.19) are given by

$$\wp = \frac{1}{2r}\left[-q \pm \sqrt{q^2 - 4pr}\right]. \tag{2.20}$$

We now consider three possible cases: $q^2 < 4pr$, $q^2 = 4pr$, and $q^2 > 4pr$.

Case A: When $q^2 < 4pr$ and $pr > 0$, the quantity $\wp$ becomes complex, meaning that Eq (2.18) has only one real root at $\psi_e = 0$. Consequently, the origin $O = (0, 0)$ is the unique equilibrium of system (2.11).

Case B: When $q^2 = 4pr$ with $pr > 0$, Eq (2.19) yields a repeated real root at $-q/(2r)$, provided that $qr < 0$. Consequently, Eq (2.18) has three real roots: $\psi_e = 0$ and $\psi_e = \pm\sqrt{-q/(2r)}$. This results in three equilibrium points for the system (2.11) as follows:

$$O = (0, 0), \qquad A_{1,2} = \left(\pm\sqrt{\frac{-q}{2r}},\ 0\right), \tag{2.21}$$

a configuration valid for either $r > 0, p > 0, q = -2\sqrt{pr}$, or $r < 0, p < 0, q = 2\sqrt{pr}$.

Case C: When $q^2 > 4pr$, the analysis splits into two sub cases sccording to the sign of pr, which we now investigate individually.

(I) If $pr < 0$, then $q^2 > 4pr$ automatically holds. The system (2.11) has three equilibrium points as follows:

$$O = (0, 0), \qquad B_{1,2} = \left(\pm\sqrt{\frac{-q + \sqrt{q^2 - 4pr}}{2r}}, 0\right), \tag{2.22}$$

for $r > 0, p < 0$. Similarly, for $r < 0, p > 0$, the equilibrium points are

$$O = (0, 0), \qquad C_{1,2} = \left(\pm\sqrt{\frac{-q - \sqrt{q^2 - 4pr}}{2r}}, 0\right). \tag{2.23}$$

(II) If $pr > 0$, then $q > 2\sqrt{pr} > 0$ or $q < -2\sqrt{pr} < 0$. The possible cases are as follows:

(a) For $r > 0, p > 0, q > 2\sqrt{pr}$, the origin $O = (0, 0)$ is the only equilibrium point.

(b) For $r > 0, p > 0, q < -2\sqrt{pr}$, the system admits five equilibrium points

$$O = (0, 0), \quad D_{1,2} = \left(\pm\sqrt{\frac{-q + \sqrt{q^2 - 4pr}}{2r}}, 0\right), \quad F_{1,2} = \left(\pm\sqrt{\frac{-q - \sqrt{q^2 - 4pr}}{2r}}, 0\right). \tag{2.24}$$

(c) For $r < 0, p < 0, q > 2\sqrt{pr}$, five equilibrium points also exist, as in Eq (2.24).

(d) For $r < 0, p < 0, q < -2\sqrt{pr}$, the system has a single equilibrium point, $O = (0, 0)$.

To ensure clarity and avoid confusion, we now present the following existence theorems.

Theorem 2. *(Existence of a unique equilibrium) The dynamic system* (2.11) *possesses a unique equilibrium point, located at the origin, if one of the following conditions holds:*

(a) $p > 0$, $r > 0$, *and* $q \in (-2\sqrt{pr},\ 2\sqrt{pr})$;

(b) $p > 0$, $r > 0$, *and* $q > 2\sqrt{pr}$;

(c) $p < 0$, $r < 0$, *and* $q \in (-2\sqrt{pr},\ 2\sqrt{pr})$;

(d) $p < 0$, $r < 0$, *and* $q < -2\sqrt{pr}$.

Theorem 3. *(Existence of three equilibria) The dynamic system* (2.11) *possesses exactly three distinct equilibrium points in the following cases:*

(a) Points $O = (0, 0)$ *and* $A_{1,2} = \left(\pm\sqrt{\frac{-q}{2r}},\ 0\right)$ *exist when either* $r > 0$, $p > 0$, *and* $q = -2\sqrt{pr}$ *or* $r < 0$, $p < 0$, *and* $q = 2\sqrt{pr}$.

(b) Points $O = (0, 0)$ *and* $B_{1,2} = \left(\pm\sqrt{\frac{-q+\sqrt{q^2-4pr}}{2r}},\ 0\right)$ *exist when* $p < 0$ *and* $r > 0$.

(c) Points $O = (0, 0)$ *and* $C_{1,2} = \left(\pm\sqrt{\frac{-q-\sqrt{q^2-4pr}}{2r}},\ 0\right)$ *exist when* $p > 0$ *and* $r < 0$.

Theorem 4. *(Existence of five equilibria) The dynamic system* (2.11) *has five distinct equilibrium points*

$$O = (0, 0), \quad D_{1,2} = \left(\pm\sqrt{\frac{-q+\sqrt{q^2-4pr}}{2r}},\ 0\right), \quad F_{1,2} = \left(\pm\sqrt{\frac{-q-\sqrt{q^2-4pr}}{2r}},\ 0\right),$$

under either one of the parameter conditions $r > 0$, $p > 0$, *and* $q < -2\sqrt{pr}$, *or* $r < 0$, $p < 0$, *and* $q > 2\sqrt{pr}$ *is verified.*

We now determine the nature of these point by using the Lagrange Theorem 1; consequently, we compute

$$\frac{d^2V}{d\psi^2}(\psi_e) = p + 3q\psi_e + 5r\psi_e^4. \tag{2.25}$$

The qualitative behavior of the system (2.11) is examined under three distinct configurations, determined by the number of equilibrium points. Specifically, the system may exhibit a single equilibrium point, three equilibrium points, or five equilibrium points. These cases are rigorously characterized in Theorems 2–4, respectively.

Case I: At the unique equilibrium point, the second derivative of the potential is $\frac{d^2V}{d\psi^2}(0) = p$. Combining this with the parameter ranges established in Theorem 2 and applying the stability criteria of Lagrange's Theorem 1, we can classify the equilibrium point O as follows.

- The origin O is a center when $p > 0$, $r > 0$, and $q \in (-2\sqrt{pr}, 2\sqrt{pr}) \cup (2\sqrt{pr}, \infty)$. The corresponding phase portrait is shown in Figure 1(a).
- Conversely, O is a saddle point when $p < 0$, $r < 0$, and $q \in (-2\sqrt{pr}, 2\sqrt{pr}) \cup (-\infty, -2\sqrt{pr})$. The phase portrait for this scenario is depicted in Figure 1(b).

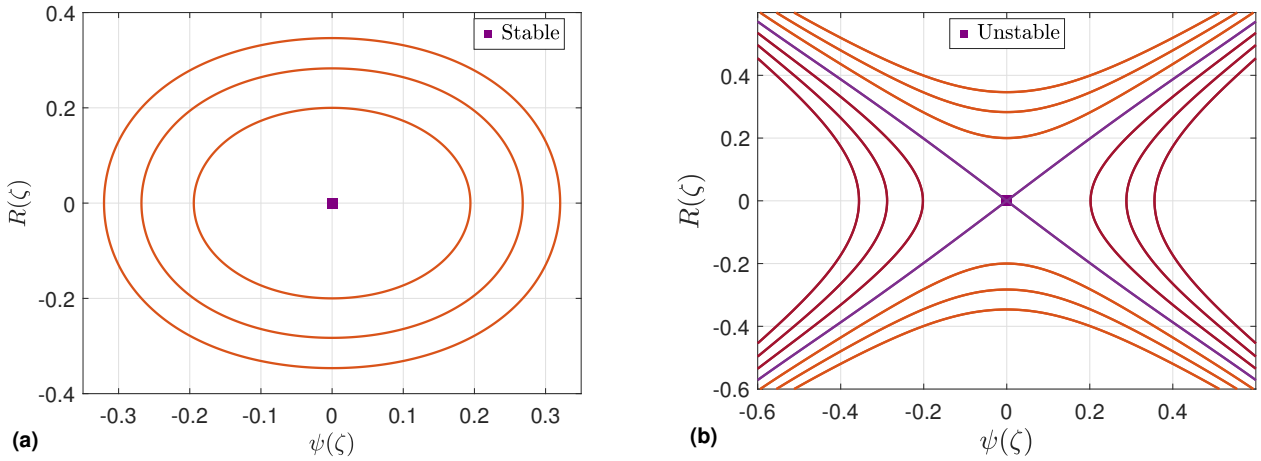

Figure 1. Phase portrait of the system (2.11) with a unique equilibrium point at the origin. **(a)** A center, for the parameters $p, r > 0$ and $q \in (-2\sqrt{pr}, 2\sqrt{pr}) \cup (2\sqrt{pr}, \infty)$. **(b)** A saddle point, for the parameters $p, r < 0$ and $q \in (-2\sqrt{pr}, 2\sqrt{pr}) \cup (-\infty, -2\sqrt{pr})$.

Case II: We now analyze the case where the system (2.11) possesses three equilibrium points, as established in Theorem 3. The three subcases outlined in the theorem are examined individually.

(a) According to Part (a) of Theorem 3, the system (2.11) possesses the three equilibrium points O and $A_{1,2}$. To classify their stability using Lagrange's theorem, we compute the second derivatives:

$$\frac{d^2V}{d\psi^2}(0) = p, \quad \frac{d^2V}{d\psi^2}\left(\pm\sqrt{\frac{-q}{2r}}\right) = 0. \tag{2.26}$$

From this, it follows that the non trivial points $A_{1,2}$ are always cusps. The nature of the origin O, however, depends on the parameters.

- For $r > 0$, $p > 0$, and $q = -2\sqrt{pr}$, the point O is a center. The corresponding phase portrait is shown in Figure 2(a).
- For $r < 0$, $p < 0$, and $q = 2\sqrt{pr}$, the point O is a saddle. This case is illustrated by the phase portrait in Figure 2(b).

(b) In accordance with Part (b) of Theorem 3, the system (2.11) possesses three equilibrium points: the origin, O, and two symmetric points, $B_{1,2}$. To ascertain their stability, we first compute the second derivative of the function V with respect to ψ at these points. This yields the following results:

$$\frac{d^2V}{d\psi^2}(0) = p, \quad \frac{d^2V}{d\psi^2}\left(\pm\sqrt{\frac{-q+\sqrt{q^2-4pr}}{2r}}\right) = \frac{q^2-4pr+q\sqrt{q^2-4pr}}{r}. \tag{2.27}$$

Applying the criteria from Lagrange's Theorem 1, we can deduce the stability of these points. Specifically, the equilibrium point O is a saddle point, whereas the points $B_{1,2}$ are centers. This stability configuration holds true under the conditions $p < 0$ and $r > 0$, with the condition $q^2 > 4pr$ being automatically satisfied. The resulting phase portrait for this specific case is illustrated in Figure 2(c).

(c) According to Part (c) of Theorem 3, the system (2.11) has three equilibrium points O and $C_{1,2}$ when $p > 0$, $r < 0$, and $q^2 > 4pr$. To determine the nature of these points, we apply Lagrange's Theorem 1. We calculate

$$\frac{d^2V}{d\psi^2}(0) = p, \quad \frac{d^2V}{d\psi^2}\left(\pm\sqrt{\frac{-q-\sqrt{q^2-4pr}}{2r}}\right) = \frac{q^2-4pr+q\sqrt{q^2-4pr}}{r}. \tag{2.28}$$

From these calculations, we conclude that point O is a center, while the two equilibrium points $C_{1,2}$ are saddle points. Figure 2(d) illustrates the phase portrait for this case.

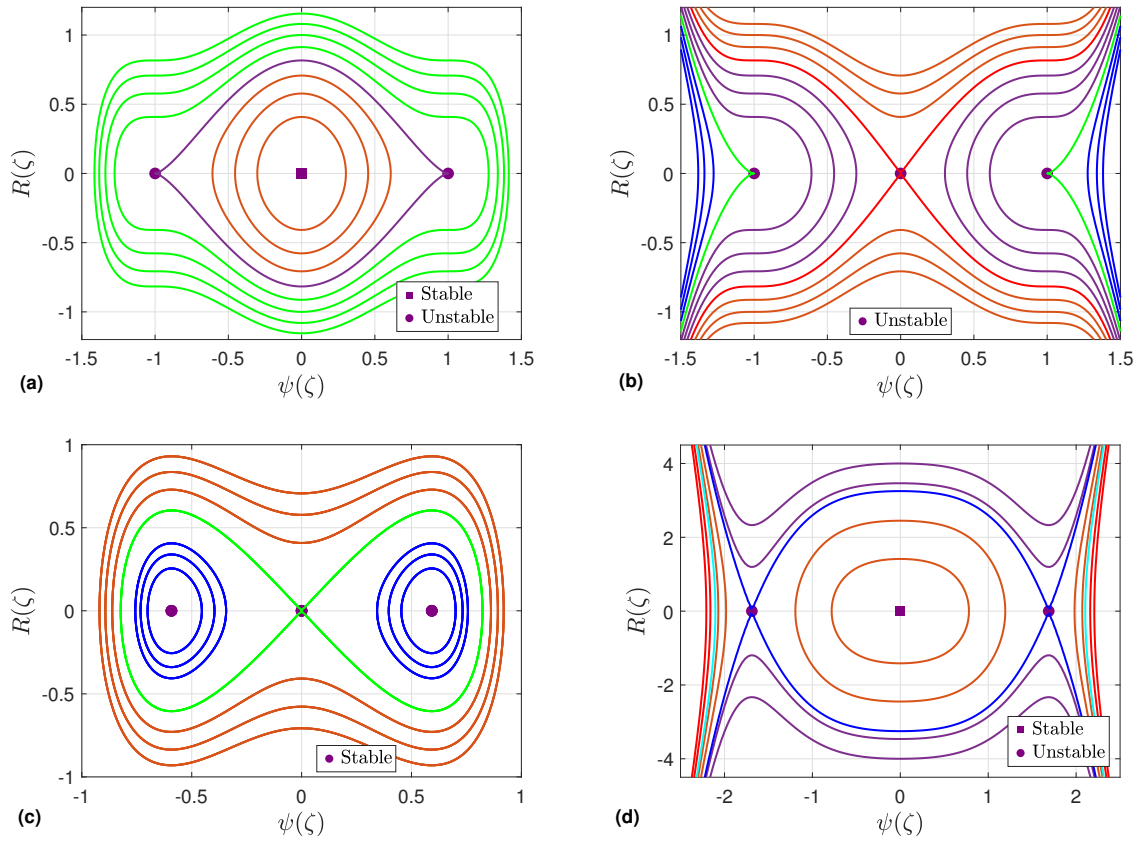

Figure 2. Phase portrait of the system (2.11) when it has three equilibria. **(a)** $r > 0, p > 0$, and $q = -2\sqrt{pr}$. **(b)** $r < 0, p < 0$, and $q = 2\sqrt{pr}$. **(c)** $p < 0, r > 0$, and $q^2 > 4pr$. **(d)** $p > 0, r < 0$, and $q^2 > 4pr$.

Case III: According to Theorem 4, the system (2.11) has five equilibrium points O, $D_{1,2}$, and $F_{1,2}$ when either $r > 0$, $p > 0$, and $q < -2\sqrt{pr}$ or $r < 0$, $p < 0$, and $q > 2\sqrt{pr}$ holds. To determine their stability, we evaluate

$$\begin{aligned} &\frac{d^2V}{d\psi^2}(0) = p, \quad \frac{d^2V}{d\psi^2}\left(\pm\sqrt{\frac{-q+\sqrt{q^2-4pr}}{2r}}\right) = \frac{q^2-4pr-q\sqrt{q^2-4pr}}{r}, \\ &\frac{d^2V}{d\psi^2}\left(\pm\sqrt{\frac{-q-\sqrt{q^2-4pr}}{2r}}\right) = \frac{q^2-4pr+q\sqrt{q^2-4pr}}{r}. \end{aligned} \tag{2.29}$$

When $r > 0$, $p > 0$, $q < -2\sqrt{pr}$, the equilibrium points O and $D_{1,2}$ are centers, while the points $F_{1,2}$ are saddle points. Figure 3(a) illustrates the phase portrait for this case. When $r < 0$, $p < 0$, and $q > 2\sqrt{pr}$, the equilibrium points O and $F_{1,2}$ are saddle points, while the points $D_{1,2}$ are centers. Figure 3(b) depicts the phase portrait for this case.

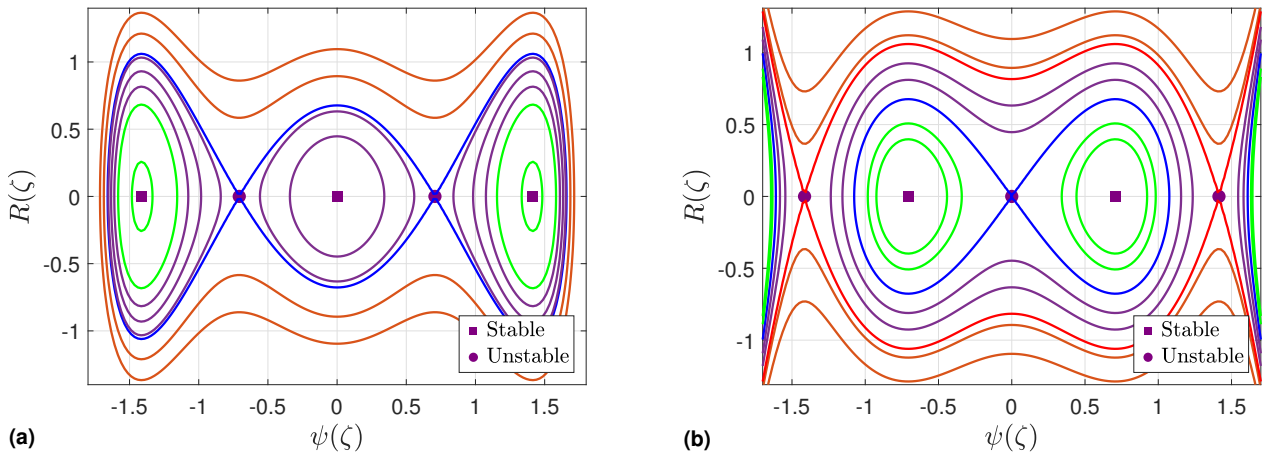

Figure 3. Phase portrait of the system (2.11) corresponding to the case $q^2 > 4pr$ with $pr > 0$ (a)$r > 0$, $p > 0$, and $q < -2\sqrt{pr}$ and (b) $r < 0$, $p < 0$, and $q > 2\sqrt{pr}$.

To avoid confusion, we summarize the parameter regimes and the corresponding phase portrait characteristics in Table 1.

Table 1. Parameter regimes and corresponding phase portrait characteristics. Set $u = 2\sqrt{pr}$ if $pr > 0$.

No.	Conditions on			Phase portrait			Bifurcation type	Description
	p	r	q	Equilibria	Stability	Figure	Present	
1.	+	+	$(-u, u)$ $\cup(u, \infty)$	O	Center	1(a)	No local bifurcation	All orbits are bounded and form periodic orbits around O.
2.	−	−	$(-u, u)$ $\cup(-\infty, -u)$	O	Center	1(b)	No local bifurcation	All orbits are un- bounded
3.	+	+	$\{-u\}$	O	Center	2(a)	Saddle node (degenerate)	Bounded periodic orbits around O, separated by a separatrix connecting the cusps.
				$A_{1,2}$	Cusp			
4.	−	−	$\{u\}$	O	Saddle	2(b)	Saddl node (degenerate)	All orbits are unbounded
				$A_{1,2}$	Cusp			
5.	−	+	$q^2 > 4pr$	O	Saddle	2(c)	Homoclinic bifurcation at $\nu = 0$	Two families of periodic orbits around O, separated by a homoclinic loop to O.
				$B_{1,2}$	Center			
6.	+	−	$q^2 > 4pr$	O	Center	2(d)	Heteroclinic bifurcation at $\nu = \nu_C$	Periodic orbits around O bounded by a heteroclinic connecting joining C_1 and C_2.
				$C_{1,2}$	Saddle			
7.	+	+	$q < -u$	O	Center	3(a)	Saddle node and heteroclinic	Three families of periodic orbits (one around each center) separated by heteroclinic cycles connecting F_1 and F_2.
				$D_{1,2}$	Center			
				$F_{1,2}$	Saddle			
8.	−	−	$q > u$	O	Saddle	3(b)	Saddle node and homoclinic	Two families of periodic orbits around $D_{1,2}$, with each enclosed loop to $F_{1,2}$; unbounded orbits elsewhere.
				$D_{1,2}$	Center			
				$F_{1,2}$	Saddle			

2.1. Phase portrait description

This subsection provides a concise description of the system's phase portraits. The phase orbits are curves parameterized by the energy level ν, given by

$$\mathcal{P}_\nu = \left\{(\psi, \psi') \in \mathbb{R}^2 : \psi' = \pm\sqrt{2(\nu - V(\psi))}\right\}. \tag{2.30}$$

To characterize these orbits, we compute the Hamiltonian's value at the equilibrium points as follows:

$$\nu_O = \mathcal{H}(O), \quad \nu_A = \mathcal{H}(A_{1,2}), \quad \nu_B = \mathcal{H}(B_{1,2}), \quad \nu_C = \mathcal{H}(C_{1,2}), \quad \nu_D = \mathcal{H}(D_{1,2}), \quad \nu_F = \mathcal{H}(F_{1,2}). \tag{2.31}$$

(a) For $(p, r, q) \in \mathbb{R}^+ \times \mathbb{R}^+ \times \left((-2\sqrt{pr}, 2\sqrt{pr}) \cup (2\sqrt{pr}, \infty)\right)$, the phase portrait is shown in Figure 1(a). It features a single equilibrium point O, which is a stable center, surrounded by a family of periodic orbits $\mathcal{P}_{\nu>0}$. This family of orbits shrinks and degenerates into the point O as $\nu \to 0$.

(b) For $(p, r, q) \in \mathbb{R}^- \times \mathbb{R}^- \times \left((-2\sqrt{pr}, 2\sqrt{pr}) \cup (-\infty, -2\sqrt{pr})\right)$, the phase portrait is shown in Figure 1(b). It is composed of a single saddle equilibrium point O and various unbounded orbits for different values of ν: $\mathcal{P}_{\nu=0}$ (purple), $\mathcal{P}_{\nu>0}$ (gold), and $\mathcal{P}_{\nu<0}$ (brown). The orbit $\mathcal{P}_{\nu=0}$ is a limiting orbit, as the gold and brown families approach it when $\nu \to 0$.

(c) For the parameter values $r > 0$, $p > 0$, and $q = -2\sqrt{pr}$, the phase portrait of the system (2.11) is depicted in Figure 2(a). The system possesses three equilibrium points: A center at O and two saddle points at $A_{1,2}$. All phase orbits are bounded and consist of two families of periodic orbits—shown in green ($\mathcal{P}_{\nu>\nu_A}$) and gold ($\mathcal{P}_{0<\nu<\nu_A}$)—which are separated by the purple limiting orbit $\mathcal{P}_{\nu=\nu_A}$.

(d) The phase portrait for the system (2.11) with the parameters $r < 0$, $p < 0$, and $q = 2\sqrt{pr}$ features three equilibrium points: a saddle at O and two cusps at $A_{1,2}$, as shown in Figure 2(b). It contains several families of unbounded orbits for different energy levels ν: the gold orbits $\mathcal{P}_{0<\nu<\nu_A}$, the purple orbits $\mathcal{P}_{\nu_A<\nu<0}$, the red orbit $\mathcal{P}_{\nu=0}$, and the green orbit $\mathcal{P}_{\nu=\nu_A}$.

(e) When $p < 0, r > 0$, and $q^2 > 4pr$, the phase portrait for the system (2.11) is clarified by Figure 2(c). It composed of three equilibrium points: O (saddle) and $B_{1,2}$ (center). All phase plane orbits are bounded. There is a family of super-periodic orbits in gold that is characterized by $\mathcal{P}_{\nu>0}$ and two families of periodic orbits in blue characterized by $\mathcal{P}_{\nu_B<\nu<0}$ and these families are separated by the limited homoclinic green orbit $\mathcal{P}_{\nu=0}$. It is obvious that when the parameter ν tends to zero, the super periodic family in gold and the two periodic families in blue degenerate to the homoclinic orbit in green. When ν tends to ν_B, the two periodic families of orbits will degenerate into the two centers points $B_{1,2}$.

(f) The phase portrait for the system (2.11) is displayed in Figure 2(d) for the parameters $p > 0$, $r < 0$, and $q^2 > 4pr$. It is composed of three equilibrium points: a center at O and saddle points at $C_{1,2}$. The portrait features a family of gold orbits $\mathcal{P}_{0<\nu<\nu_C}$, which itself consists of three distinct types: Two unbounded families lying outside the blue heteroclinic orbit $\mathcal{P}_{\nu=\nu_C}$, and one periodic family enclosed by it. The remaining phase orbits are all unbounded, categorized as $\mathcal{P}_{\nu_C<\nu<\infty}$ (purple), $\mathcal{P}_{\nu=0}$ (cyan), and $\mathcal{P}_{-\infty<\nu<0}$ (red). As $\nu \to 0$, the periodic gold family degenerates to the center point O. As $\nu \to \nu_C$, this same family degenerates into the blue heteroclinic orbit.

(g) The phase portrait for the system (2.11) is shown in Figure 3(a) for the parameters $r > 0$, $p > 0$, and $q < -2\sqrt{pr}$. It consists of five equilibrium points: Centers at O and $D_{1,2}$, and saddle points at $F_{1,2}$. All phase orbits are bounded. The structure includes several distinct families: a family of super-periodic gold orbits ($\mathcal{P}_{\nu>\nu_F}$), two families of green periodic orbits encircling the centers $D_{1,2}$ ($\mathcal{P}_{\nu_D<\nu<\nu_F}$), and three families of purple periodic orbits around the centers O and $D_{1,2}$ ($\mathcal{P}_{0<\nu<\nu_F}$). These are separated by a blue heteroclinic orbit, characterized by $\mathcal{P}_{\nu=\nu_F}$, which connects the two saddle points $F_{1,2}$. As $\nu \to \nu_F$, both the super-periodic gold family and the three purple periodic families degenerate into this blue heteroclinic cycle.

(h) Figure 3(b) shows the phase portrait for the system (2.11) with the parameters $r < 0$, $p < 0$, and $q > 2\sqrt{pr}$. The portrait features five equilibrium points: Saddle points at O and $F_{1,2}$, and centers at $D_{1,2}$. The orbital structure includes green orbits ($\mathcal{P}_{\nu_D<\nu<0}$) consisting of two bounded, periodic families inside the two blue homoclinic orbits ($\mathcal{P}_{\nu=0}$), as well as unbounded families outside them. This is accompanied by a super-periodic family of purple orbits ($\mathcal{P}_{0<\nu<\nu_F}$), a red heteroclinic orbit ($\mathcal{P}_{\nu=\nu_F}$) connecting the two saddle points $F_{1,2}$, and unbounded gold orbits ($\mathcal{P}_{\nu>\nu_F}$). As $\nu \to 0$, the periodic green families and the super-periodic purple family degenerate into the blue homoclinic orbits. As $\nu \to \nu_D$, the two periodic green families shrink into the center points $D_{1,2}$.

It is now more appropriate to summarize the existence conditions of the periodic, solitary, and kink (or anti-kink) solutions in tabular form to enhance clarity for the reader. Tables 2–4 list these existence conditions accordingly.

Table 2. Conditions of existence of all periodic solutions. Set $u = 2\sqrt{pr}$ if $pr > 0$.

No.	Conditions on			Range of	Phase portrait		Graph of	No. of real
	p	r	q	ν	Figure	Color	$\mathcal{M}$	Roots to $\mathcal{M}$
1.	+	+	$(-u, u) \cup (u, \infty)$	+	1(a)	Gold	4(a)	2
2.	+	+	$\{-u\}$	$(0, \nu_A)$	2(a)	Gold	4(a)	2
				(ν_A, ∞)		Green		
3.	−	+	$q^2 > 4pr$	$(\nu_B, 0)$	2(c)	Blue	4(b)	4
				$(0, \infty)$		Gold	4(a)	2
4.	+	−	$q^2 > 4pr$	$(0, \nu_C)$	2(d)	Gold	4(c)	4
5.	+	+	$q < -u$	$(0, \nu_F)$	3(a)	Purple	4(d)	6
				(ν_F, ∞)	3(a)	Gold	4(a)	2
				(ν_D, ν_F)	3(a)	Green	4(b)	4
6	−	−	$q > 2u$	$(\nu_D, 0)$	3(b)	Green	4(f)	6
				$(0, \nu_F)$	3(b)	Purple	4(e)	4

Table 3. Conditions of existence of all solitary solutions. Set $u = 2\sqrt{pr}$ if $pr > 0$.

No.	Conditions on			Range of	Phase portrait		Graph of	No. of real
	p	r	q	ν	Figure	Color	$\mathcal{M}$	Roots to $\mathcal{M}$
1.	−	+	$q^2 > 4pr$	0	2(d)	Green	5(a)	2 simple, 1 double
2.	+	+	$q < -u$	ν_F	3(a)	Blue	6(b)	2 simple, 2 double
3.	−	−	$q > u$	ν_F	3(b)	Bblue	5(b)	4 simple, 1 double

Table 4. Conditions of existence of all kink (anti-kink) solutions. Define $u = 2\sqrt{pr}$ if $pr > 0$.

No.	Conditions on			Range of	Phase portrait		Graph of	No. of real
	p	r	q	ν	Figure	Color	$\mathcal{M}$	Roots to $\mathcal{M}$
1.	+	−	$q^2 > 4pr$	ν_C	2(d)	Blue	6(a)	2 double
2.	+	+	$(-\infty, -u)$	ν_F	3(a)	Blue	6(b)	2 simple, 2 double
3.	−	−	(u, ∞)	ν_F	3(b)	Red	5(b)	4 simple, 1 double

3. Solution

This section aims to obtain exact solutions of Eq (1.1) by integrating the conserved quantity (2.17) over specific intervals, using the bifurcation constraints on the parameters discussed in the preceding section.

Inserting the first equation in the system (2.11) into the conserved quantity (2.17) and separating the variables, we get the the following one-dimensional (1D) form:

$$\pm \mathrm{d}\zeta = \frac{\mathrm{d}\psi}{\sqrt{\mathcal{M}(\nu;\psi)}}, \tag{3.1}$$

where $\mathcal{M}(\nu;\psi)$ is a six-degree polynomial in ψ and has the form

$$\mathcal{M}(\nu;\psi) = 2\nu - p\psi^2 - \frac{q}{2}\psi^4 - \frac{r}{3}\psi^6. \tag{3.2}$$

To integrate the 1D form given by Eq (3.1), we must first establish the valid ranges for the parameters p, q, r, and ν and identify the intervals where real solutions can be formed. This is where bifurcation analysis becomes essential. Its importance lies not only in defining these requirements but also in its capacity to classify solution types before explicitly deriving them. For example, the existence of periodic, homoclinic, and heteroclinic orbits in the phase plane directly signals the presence of periodic, solitary, and kink (or anti-kink) wave solutions, respectively. Furthermore, this analysis allows us to filter out unbounded solutions, which correspond to unbounded phase orbits. Since such unbounded solutions are typically non physical, identifying and excluding them is a critical step in the process. Therefore, we restrict our attention to bounded solutions. To find real solutions, one must first identify the intervals where wave propagation is physically possible. These intervals, which correspond to the real motion of the Hamiltonian system (2.11), are identified by studying the roots of the polynomial $\mathcal{M}$. In other words, these intervals are equivalent to find the solution of the inequality $\mathcal{M} > 0$. Therefore, we examine the graph of $\mathcal{M}$ for different choices of the parameters p, q, r, and ν in order to determine these ranges and to interpret their physical meaning. Figure 4 presents the polynomial (3.2) for those values of ν, p, q, and r that give rise to periodic orbits, and is used to determine the intervals of real, bounded periodic solutions. Figure 5 displays the polynomial (3.2) for parameter values that generate a homoclinic phase orbit. Figure 6 depicts the polynomial (3.2) for all admissible values of ν, p, q, and r leading to bounded kink (or antikink) solutions associated with heteroclinic phase orbits. In these plots, the regions corresponding to bounded solutions are shaded in cyan, whereas the pink regions indicate real unbounded solutions, which are of lesser physical relevance.

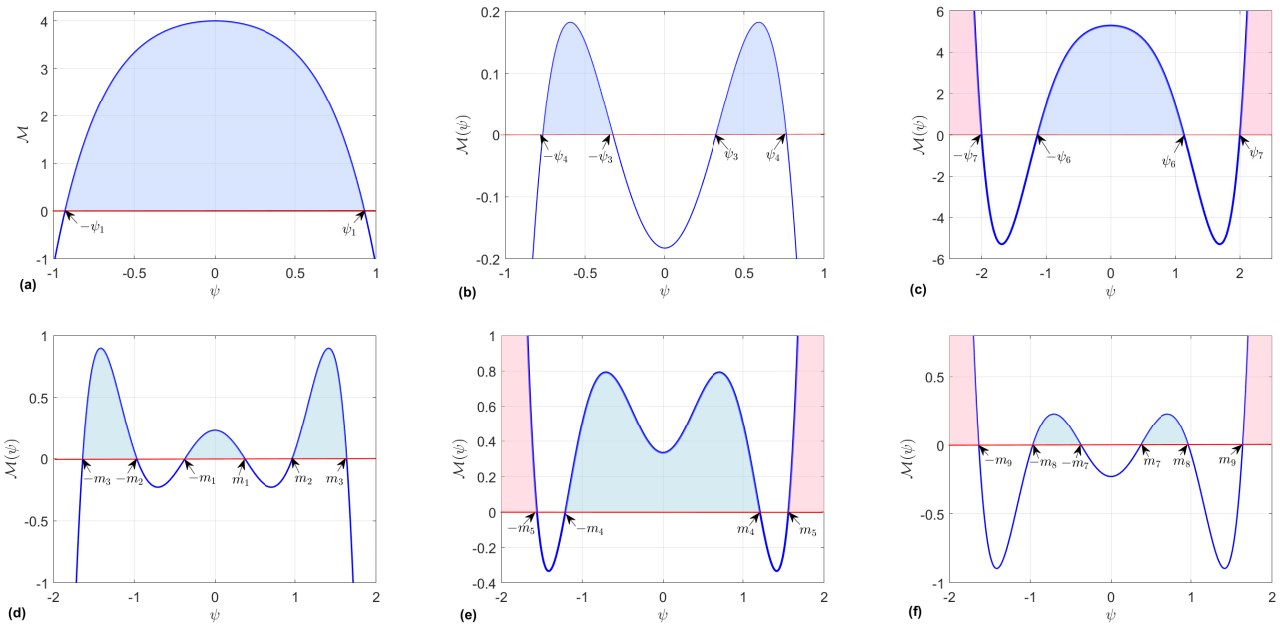

Figure 4. The graph of $\mathcal{M}$ for different values of system (2.11) in the case of periodic solutions. The cyan and pink regions refers to region of possible real propagation and region of unbounded solutions.

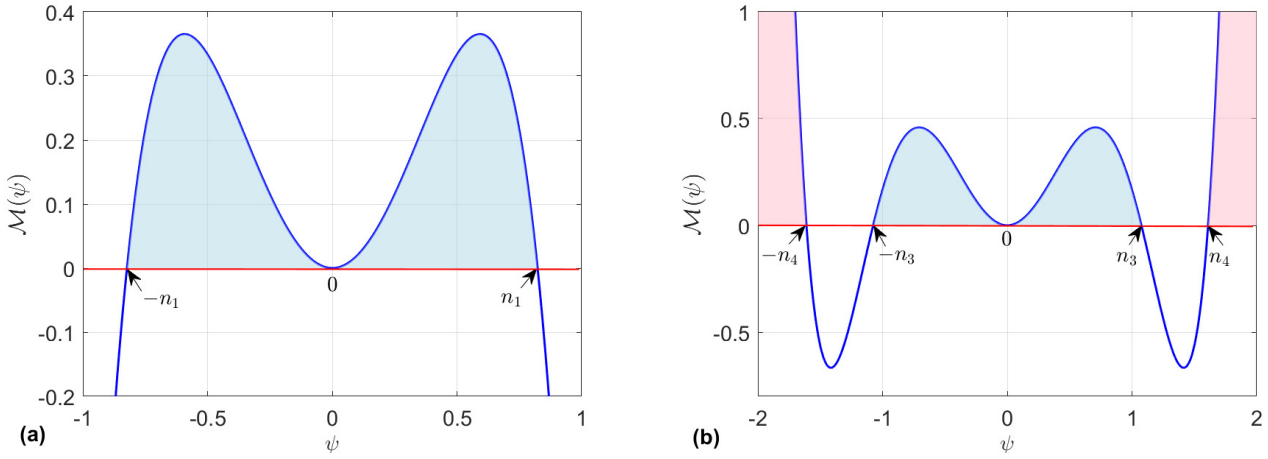

Figure 5. The graph of $\mathcal{M}$ for different values of the the system (2.11) in the case of solitary solutions. The cyan and pink region refer to the region of possible real propagation and the region of unbounded solutions.

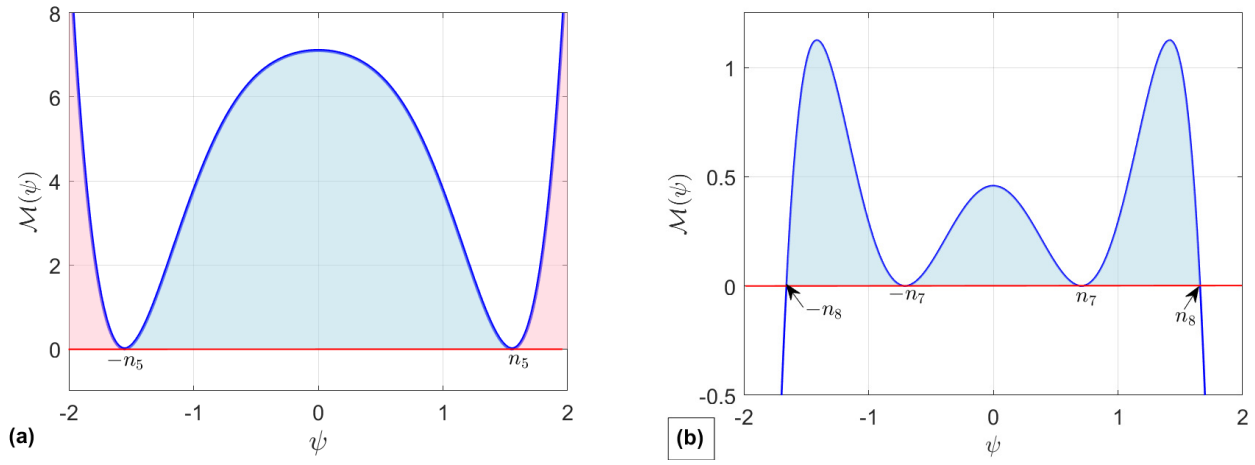

Figure 6. The graph of $\mathcal{M}$ for different values of the system (2.11) in the case of kink (or anti-kink) solutions. The cyan and pink region refers to the region of possible real propagation and the region of unbounded solutions.

3.1. Periodic solutions

The bifurcation analysis reveals that periodic solutions arise for various values of the parameters p, q, r, and v. Each case is considered separately below.

(a) When $v > 0$, $r > 0$, $p > 0$, and $q \in (-2\sqrt{pr}, 2\sqrt{pr}) \cup (2\sqrt{pr}, \infty)$, the polynomial (3.2) possesses only two real roots, $\pm\psi_1$ (with $\psi_1 > 0$), along with a pair of complex conjugate roots, as illustrated in Figure 4(a). Consequently, it can be factored as

$$\mathcal{M} = \frac{r}{3}(\psi_1^2 - \psi^2)\left[(\psi - \gamma_0)^2 + \rho_0^2\right]\left[(\psi + \gamma_0)^2 + \rho_0^2\right].$$

The interval supporting real solutions is therefore $\psi \in (-\psi_1, \psi_1)$ (see Figure 4(a)). Assuming the initial condition $\psi(0) = 0$ and integrating the 1D form (3.1), we derive the expression:

$$\psi(\zeta) = \psi_1 \sqrt{\frac{\varrho_1}{\varrho_1 - \varrho_2}\left[1 - \frac{2\varrho_1}{\varrho_1 + \varrho_2 + (\varrho_1 - \varrho_2)\,\mathrm{cn}(\Omega_1\zeta, \kappa_1)}\right]}, \tag{3.3}$$

where $\mathrm{cn}(\cdot,\cdot)$ denotes a Jacobi elliptic function [33], $\Omega_1 = \sqrt{\frac{4r\varrho_1\varrho_2}{3}}$, $\kappa_1 = \sqrt{\frac{\psi_1^2 - \varrho_1 + \varrho_2}{4\varrho_1\varrho_2}}$, $\varrho_1 = \gamma_0^2 + \rho_0^2$, and $\varrho_2 = -\sqrt{(\psi_1^2 + \varrho_1)^2 - 4\gamma_0^2\psi_1^2}$.

Substituting (3.3) into (2.8) yields

$$\begin{aligned}\mu_1(\zeta) = &\frac{3}{16a_1(\varrho_1-\varrho_2)\Omega_1\sqrt{(\varrho_1-\varrho_2)^2+4\kappa_1^2\varrho_1\varrho_2}}\Big[a_5\psi_1^2\sqrt{-4\varrho_1\varrho_2}\\ &\times\ln\left(\frac{\sqrt{(\varrho_1-\varrho_2)^2+4\kappa_1^2\varrho_1\varrho_2}\,\mathrm{sn}(\Omega_1\zeta,\kappa_1)+2\sqrt{-\varrho_1\varrho_2}\,\mathrm{dn}(\Omega_1\zeta,\kappa_1)}{\sqrt{(\varrho_1-\varrho_2)^2+4\kappa_1^2\varrho_1\varrho_2}\,\mathrm{sn}(\Omega_1\zeta,\kappa_1)-2\sqrt{-\varrho_1\varrho_2}\,\mathrm{dn}(\Omega_1\zeta,\kappa_1)}\right)\\ &-2\sqrt{(\varrho_1-\varrho_2)^2+4\kappa_1^2\varrho_1\varrho_2}\left\{a_5\psi_1^2(\varrho_1+\varrho_2)\,\Pi\left(\mathrm{sn}(\Omega_1\zeta,\kappa_1),\frac{-(\varrho_1-\varrho_2)^2}{4\varrho_1\varrho_2},\kappa_1\right)\right.\\ &\left.-\frac{2\Omega_1}{3}\left[(3a_5\psi_1^2-4a_1\beta-2\varpi)\varrho_2+2\varrho_1(2a_1\beta+\varpi)\right]\zeta\right\}\Big],\end{aligned} \tag{3.4}$$

where $\Pi(\cdot,\cdot,\cdot)$ is the incomplete elliptic integral of the third kind [33].

Thus, Eq (1.1) admits the solution

$$\phi_1(\zeta)=\psi_1\sqrt{\frac{\varrho_1}{\varrho_1-\varrho_2}\left[1-\frac{2\varrho_1}{\varrho_1+\varrho_2+(\varrho_1-\varrho_2)\,\mathrm{cn}(\Omega_1\zeta,\kappa_1)}\right]}\exp\left[i(\alpha t-\beta x)+i\mu_1(\zeta)\right]. \tag{3.5}$$

To the best of our knowledge, the solution (3.5) is novel and has not been previously reported in the literature.

(b) For the parameter set where $r>0$, $p>0$, $q=-2\sqrt{pr}$, and $\nu\in(0,\nu_A)\cup(\nu_A,\infty)$, the polynomial $\mathcal{M}$ yields precisely two real roots, with the remainder forming a complex conjugate pair (see Figure 2(a)). This is reflected in the phase portrait, where the green and gold trajectories intersect the ψ-axis at only two distinct points. Consequently, Eq (1.1) admits a solution of the same functional form as (3.5), but with the arguments derived from the new root structure of $\mathcal{M}$.

A similar situation occurs for $r>0$, $p<0$, $q^2>4pr$, and $\nu\in(0,\infty)$, where a super-periodic orbit (shown in gold in Figure 2(c)) appears. Each orbit in this family also crosses the ψ-axis at two points. Thus, the corresponding solution for Eq (1.1) is again given by the form in (3.5) with appropriately modified parameters. These solutions, while sharing the periodic structure of (3.5), are classified as super- periodic because of their distinct parameter regime and orbital characteristics.

(c) When $p<0$, $r>0$, $q^2\geq 4pr$, and $\nu\in(\nu_B,0)$, the system (2.11) exhibits two families of periodic orbits, shown in blue in Figure 2(c). A single orbit from either family intersects the ψ-axis at two points, indicating that the polynomial $\mathcal{M}$ possesses four real roots $\pm\psi_3$, $\pm\psi_4$ (with $0<\psi_3<\psi_4$) and two purely imaginary roots $\pm i\psi_5$ ($\psi_5>0$), as confirmed by Figure 4(b). Consequently, the polynomial can be expressed as $\mathcal{M}=\frac{r}{3}(\psi_3^2-\psi^2)(\psi^2-\psi_4^2)(\psi^2+\psi_5^2)$. The intervals supporting real solutions are $\psi\in(\psi_3,\psi_4)\cup(-\psi_4,-\psi_3)$, as shown in Figure 4(b). The first interval corresponds to the right- hand periodic family, while the second is associated with the left- hand family. Integrating the 1D form (3.1) with the initial condition $\psi(0)=\psi_3$ yields

$$\psi(\zeta)=\frac{\psi_3\psi_4}{\sqrt{\psi_4^2+(\psi_3^2-\psi_4^2)\,\mathrm{sn}^2(\Omega_2\zeta,\kappa_2)}}, \tag{3.6}$$

where $\Omega_2 = \psi_4\sqrt{\frac{r}{3}(\psi_3^2+\psi_5^2)}$ and $\kappa_2 = \frac{\psi_5}{\psi_4}\sqrt{\frac{\psi_4^2-\psi_3^2}{\psi_3^2+\psi_5^2}}$. Substituting the expression of (3.6) into (2.8) gives

$$\mu_2(\zeta) = \frac{2a_1\beta+\varpi}{2a_1}\zeta - \frac{3a_5\psi_3^2}{4a_1\Omega_2}\,\Pi\left(\mathrm{sn}(\Omega_2\zeta,\kappa_2),\ 1-\frac{\psi_3^2}{\psi_4^2},\ \kappa_2\right). \tag{3.7}$$

Consequently, Eq (1.1) admits a new solution of the form

$$\phi_2(\zeta) = \frac{\psi_3\psi_4}{\sqrt{\psi_4^2+(\psi_3^2-\psi_4^2)\,\mathrm{sn}^2(\Omega_2\zeta,\kappa_2)}}\,\exp\left[i(\alpha t-\beta x)+i\mu_2(\zeta)\right]. \tag{3.8}$$

(d) If $p > 0$, $r < 0$, $q^2 > 4pr$, and $\nu \in (0,\nu_C)$, the system (2.11) exhibits two distinct families of orbits: One periodic and the other unbounded, as shown in gold in Figure 2(d). The corresponding polynomial $\mathcal{M}$ has four real roots $\pm\psi_6$, $\pm\psi_7$ (with $0 < \psi_6 < \psi_7$) and two imaginary roots $\pm i\psi_8$ ($\psi_8 > 0$), as illustrated in Figure 4(c). It can therefore be expressed as $\mathcal{M} = \frac{-r}{3}(\psi^2-\psi_6^2)(\psi^2-\psi_7^2)(\psi^2+\psi_8^2)$. Real solutions exist for $\psi \in (-\infty,-\psi_7)\cup(-\psi_6,\psi_6)\cup(\psi_7,\infty)$, as shown in Figure 4(c). The first and third intervals correspond to the unbounded orbits (pink in Figure 4(c)) and are disregarded. We consider only the second interval, which is associated with the periodic orbits. Integrating the 1D form (3.1) with the initial condition $\psi(0) = 0$ yields

$$\psi(\zeta) = \psi_8\sqrt{-1+\frac{\psi_6^2+\psi_8^2}{\psi_6^2+\psi_8^2-\psi_6^2\,\mathrm{sn}^2(\Omega_3\zeta,\kappa_3)}}, \tag{3.9}$$

where $\Omega_3 = \psi_7\sqrt{\frac{-r}{3}(\psi_6^2+\psi_8^2)}$ and $\kappa_3 = \frac{\psi_6}{\psi_7}\sqrt{\frac{\psi_7^2+\psi_8^2}{\psi_6^2+\psi_8^2}}$. Substituting (3.9) into (2.8) gives

$$\mu_3(\zeta) = \left(a_1\beta+\frac{\varpi}{2}+\frac{3a_5\psi_8^2}{4}\right)\frac{\zeta}{a_1} - \frac{3a_5\psi_8^2}{4a_1\Omega_3}\,\Pi\left(\mathrm{sn}(\Omega_3\zeta,\kappa_3),\ \frac{\psi_6^2}{\psi_6^2+\psi_8^2},\ \kappa_3\right). \tag{3.10}$$

Hence, Eq (1.1) admits a new solution of the form

$$\phi_3(\zeta) = \psi_8\sqrt{-1+\frac{\psi_6^2+\psi_8^2}{\psi_6^2+\psi_8^2-\psi_6^2\,\mathrm{sn}^2(\Omega_3\zeta,\kappa_3)}}\,\exp\left[i(\alpha t-\beta x)+i\mu_3(\zeta)\right]. \tag{3.11}$$

(e) When $r > 0$, $p > 0$, $q < -2\sqrt{pr}$, and $\nu \in (0,\nu_F)$, the system exhibits three families of periodic orbits, depicted in purple in Figure 3(a). The associated polynomial $\mathcal{M}$ possesses six real roots, $\pm m_1$, $\pm m_2$, $\pm m_3$, with $0 < m_1 < m_2 < m_3$, as shown in Figure 4(d). It can therefore be factored as $\mathcal{M} = \frac{r}{3}(m_1^2-\psi^2)(\psi^2-m_2^2)(\psi^2-m_3^2)$. Real solutions exist for $\psi \in (-m_3,-m_2)\cup(-m_1,m_1)\cup(m_2,m_3)$, as illustrated in Figure 4(d), with each interval corresponding to one of the three purple periodic families. We focus solely on the interval (m_2,m_3), as the solutions for the other intervals can be derived through similar calculations. Integrating the 1D form (3.1) with the initial condition $\psi(0) = m_2$ yields

$$\psi(\zeta) = \sqrt{m_3^2-\frac{(m_3^2-m_1^2)(m_3^2-m_2^2)}{m_3^2-m_1^2-(m_3^2-m_2^2)\,\mathrm{sn}^2(\Omega_4\zeta,\kappa_4)}}, \tag{3.12}$$

where $\Omega_4 = m_3\sqrt{\frac{r}{3}(m_3^2 - m_1^2)}$ and $\kappa_4 = \sqrt{\frac{m_3^2-m_2^2}{m_3^2-m_1^2}}$. Substituting (3.12) into (2.8) gives

$$\begin{aligned}\mu_4(\zeta) = &\left(2\varpi + 4a_1\beta - 3a_5m_3^2\right)\frac{\zeta}{4a_1}\\ &+ \frac{3a_5(m_3^2 - m_2^2)}{4a_1\Omega_4}\,\Pi\left(\mathrm{sn}(\Omega_4\zeta,\kappa_4),\ \frac{m_2^2 - m_3^2}{m_1^2 - m_3^2},\ \kappa_4\right).\end{aligned} \tag{3.13}$$

Consequently, Eq (1.1) admits a new solution of the form

$$\phi_4(\zeta) = \sqrt{m_3^2 - \frac{(m_3^2 - m_1^2)(m_3^2 - m_2^2)}{m_3^2 - m_1^2 - (m_3^2 - m_2^2)\,\mathrm{sn}^2(\Omega_4\zeta,\kappa_4)}}\,\exp\left[i(\alpha t - \beta x) + i\mu_4(\zeta)\right]. \tag{3.14}$$

(f) If $r < 0$, $p < 0$, $q > 2\sqrt{pr}$, and $\nu \in (0, \nu_F)$, the system exhibits three families of orbits, as shown in purple in Figure 3(b). Two of these families consist of unbounded orbits, while the third is composed of super periodic orbits. The corresponding polynomial $\mathcal{M}$ has four real roots, denoted by $\pm m_4$, $\pm m_5$ (with $0 < m_4 < m_5$), and two purely imaginary roots $\pm i m_6$ ($m_6 > 0$), as illustrated in Figure 4(e). Therefore, the polynomial can be written as $\mathcal{M} = -\frac{r}{3}(\psi^2 - m_4^2)(\psi^2 - m_5^2)(\psi^2 + m_6^2)$. Real solutions exist for $\psi \in (-\infty, -m_5) \cup (-m_4, m_4) \cup (m_5, \infty)$. The first and third intervals are excluded because they correspond to unbounded phase orbits (shown in pink in Figure 4(e)) and thus yield unbounded solutions. Consequently, we consider only the second interval. Integrating the 1D form (3.1) with the initial condition $\psi(0) = 0$ yields

$$\psi(\zeta) = m_6\sqrt{-1 + \frac{m_4^2 + m_6^2}{m_4^2 + m_6^2 - m_4^2\,\mathrm{sn}^2(\Omega_5\zeta,\kappa_5)}}, \tag{3.15}$$

where $\Omega_5 = m_5\sqrt{-\frac{r}{3}(m_4^2 + m_6^2)}$ and $\kappa_5 = \frac{m_4}{m_5}\sqrt{\frac{m_5^2+m_6^2}{m_4^2+m_6^2}}$. Substituting (3.15) into (2.8) gives

$$\mu_5(\zeta) = \frac{3a_5m_6^2 + 4a_1\beta + 2\varpi}{4a_1}\zeta - \frac{3a_5m_6^2}{4a_1\Omega_5}\,\Pi\left(\mathrm{sn}(\Omega_5\zeta,\kappa_5),\ \frac{m_4^2}{m_6^2 + m_4^2},\ \kappa_5\right). \tag{3.16}$$

Hence, Eq (1.1) admits a new solution of the form

$$\phi_5(\zeta) = m_6\sqrt{-1 + \frac{m_4^2 + m_6^2}{m_4^2 + m_6^2 - m_4^2\,\mathrm{sn}^2(\Omega_5\zeta,\kappa_5)}}\,\exp\left[i(\alpha t - \beta x) + i\mu_5(\zeta)\right]. \tag{3.17}$$

(g) If $r < 0$, $p < 0$, $q > 2\sqrt{pr}$, and $\nu \in (\nu_D, 0)$, the system (2.11) has four families of orbits, shown in green in Figure 3(b). Two of these families are periodic, while the other two are unbounded. The corresponding polynomial $\mathcal{M}$ possesses six real roots, $\pm m_7$, $\pm m_8$, $\pm m_9$, with $0 < m_7 < m_8 < m_9$, as illustrated in Figure 4(f). It can therefore be expressed as $\mathcal{M} = -\frac{r}{3}(\psi^2 - m_7^2)(\psi^2 - m_8^2)(\psi^2 - m_9^2)$. Real solutions exist for $\psi \in (-\infty, -m_9) \cup (-m_8, -m_7) \cup (m_7, m_8) \cup (m_9, \infty)$. The first and last intervals are associated with the unbounded solutions (pink in Figure 4(f)), while the second and

third intervals correspond to the two periodic families (cyan in Figure 4(f)). Assuming the initial condition $\psi(0) = m_8$ and integrating the 1D form (3.1), we obtain

$$\psi(\zeta) = \sqrt{m_9^2 - \frac{(m_9^2 - m_8^2)(m_9^2 - m_7^2)}{m_9^2 - m_7^2 - (m_9^2 - m_8^2)\,\mathrm{sn}^2(\Omega_6\zeta, \kappa_6)}}, \tag{3.18}$$

where $\Omega_6 = m_9\sqrt{\frac{-r}{3}(m_9^2 - m_7^2)}$ and $\kappa_6 = \sqrt{\frac{m_9^2 - m_8^2}{m_9^2 - m_7^2}}$. Substituting (3.18) into (2.8) yields

$$\mu_6(\zeta) = \frac{2\varpi + 4a_1\beta - 3a_5m_9^2}{4a_1}\zeta - \frac{3a_5(m_9^2 - m_8^2)}{4a_1\Omega_6}\,\Pi\left(\mathrm{sn}(\Omega_6\zeta, \kappa_6),\ \frac{m_8^2 - m_9^2}{m_7^2 - m_9^2},\ \kappa_6\right). \tag{3.19}$$

Consequently, Eq (1.1) admits a novel solution of the form

$$\phi_6(\zeta) = \sqrt{m_9^2 - \frac{(m_9^2 - m_8^2)(m_9^2 - m_7^2)}{m_9^2 - m_7^2 - (m_9^2 - m_8^2)\,\mathrm{sn}^2(\Omega_6\zeta, \kappa_6)}}\ \exp\left[i(\alpha t - \beta x) + i\mu_6(\zeta)\right]. \tag{3.20}$$

3.2. Solitary solution

This particular type of solution arises from the presence of a homoclinic phase orbit within the system (2.11). A homoclinic orbit is defined as a trajectory that connects a saddle equilibrium point back to itself. Let us consider the conditions on the parameters leading to solitary solutions individually.

(a) If $p < 0$, $r > 0$, $q^2 > 4pr$, and $\nu = 0$, the system admits two homoclinic trajectories, shown in green in Figure 2(c). In this parameter regime, the polynomial $\mathcal{M}$ possesses four real roots: A double root at the origin and a pair of simple roots $\pm n_1$, together with two purely imaginary roots $\pm n_2 i$, as depicted in Figure 5(a). Consequently, the polynomial may be factorized as

$$\mathcal{M} = \frac{r}{3}\,\psi^2\,(n_1^2 - \psi^2)(\psi^2 + n_2^2).$$

Real solutions occur only for $\psi \in (-n_1, 0) \cup (0, n_1)$, highlighted in cyan in Figure 5(a); each of these intervals corresponds to a distinct homoclinic orbit. We focus on the right- hand branch. Choosing the initial condition $\psi(0) = n_1$ and integrating the 1D form (3.1) yields

$$\psi(\zeta) = \frac{\sqrt{2}\,n_1n_2}{\sqrt{n_2^2 - n_1^2 + (n_1^2 - n_2^2)\cosh\left(\sqrt{\frac{r}{3}}\,n_1n_2\,\zeta\right)}}. \tag{3.21}$$

Substituting (3.21) into (2.8) gives

$$\mu_7 = \frac{2a_1\beta + \varpi}{2a_1}\,\zeta - \frac{3a_5\sqrt{3}}{2a_1\sqrt{r}}\arctan\left(\frac{n_1}{n_2}\tanh\left(\frac{\sqrt{3r}}{6}\,n_1n_2\,\zeta\right)\right). \tag{3.22}$$

Therefore, Eq (1.1) admits the solitary type solution

$$\phi_7(\zeta) = \frac{\sqrt{2}\,n_1n_2}{\sqrt{n_2^2 - n_1^2 + (n_1^2 - n_2^2)\cosh\left(\sqrt{\frac{r}{3}}\,n_1n_2\,\zeta\right)}}\ \exp\left[i(\alpha t - \beta x) + i\mu_7(\zeta)\right]. \tag{3.23}$$

(b) If $r < 0$, $p < 0$, $q > 2\sqrt{pr}$, and $\nu = 0$, the phase portrait contains four families of trajectories, as illustrated in blue in Figure 3(b). Two of these trajectories are homoclinic loops, while the remaining ones are unbounded. This structure reflects the fact that the polynomial $\mathcal{M}$ possesses a double root at the origin together with four additional simple real roots $\pm n_3$ and $\pm n_4$, where $0 < n_3 < n_4$, as depicted in Figure 5(b). In this case, the polynomial (3.2) can be written as

$$\mathcal{M} = \frac{-r}{3}\psi^2(\psi^2 - n_3^2)(\psi^2 - n_4^2).$$

The real solution exists within the intervals

$$\psi \in (-\infty, -n_4) \cup (-n_3, 0) \cup (0, n_3) \cup (n_4, \infty).$$

The two central intervals $(-n_3, 0) \cup (0, n_3)$ correspond to the homoclinic trajectories (shown in cyan in Figure 5(b)), while the remaining intervals produce unbounded orbits (shown in pink).

Assuming $\psi(0) = n_3$ and integrating Eq (3.1), we obtain

$$\psi(\zeta) = \frac{2n_3n_4}{\sqrt{(n_3^2 + n_4^2)\cosh\left(\sqrt{\frac{-r}{3}}\, n_3n_4\,\zeta\right) + 2n_3n_4\sinh\left(\sqrt{\frac{-r}{3}}\, n_3n_4\,\zeta\right) + n_4^2 - n_3^2}}. \tag{3.24}$$

Substituting (3.24) into (2.8) yields

$$\mu_8(\zeta) = \frac{2a_1\beta + \varpi}{2a_1}\,\zeta + \frac{3a_5n_4\sqrt{3}}{2a_1\sqrt{-r}\,[n_3\tanh\left(\frac{\sqrt{-3r}}{6}n_3n_4\zeta\right) + n_4]}. \tag{3.25}$$

Therefore, Eq (1.1) admits the following new solution:

$$\phi_8(\zeta) = \frac{2n_3n_4}{\sqrt{(n_3^2 + n_4^2)\cosh\left(\sqrt{\frac{-r}{3}}\, n_3n_4\,\zeta\right) + 2n_3n_4\sinh\left(\sqrt{\frac{-r}{3}}\, n_3n_4\,\zeta\right) + n_4^2 - n_3^2}}\exp[i(\alpha t - \beta x) + i\mu_8(\zeta)]. \tag{3.26}$$

3.3. Kink and anti-kink solutions

The kink or (anti-kink) solution arises when the phase portrait include a heteroclinic orbit which connects two saddle points. Therefore, we find these solutions by integrating the 1D form along the heteroclinic orbit. Thus, we consider the following cases.

(a) If $p > 0$, $r < 0$, $q^2 > 4pr$, and $\nu = \nu_C$, the system admits a heteroclinic trajectory linking the saddle points C_1 and C_2, as depicted in blue in Figure 2(d). Under these conditions, the polynomial (3.2) possesses a pair of repeated real roots corresponding to the ψ-coordinates of the equilibria, denoted by $\pm n_5$, along with two purely imaginary roots $\pm in_6$. Consequently, the polynomial can be factorized as

$$\mathcal{M} = -\frac{r}{3}(\psi^2 - n_5^2)^2(\psi^2 + n_6^2).$$

Real-valued solutions exist within the intervals $\psi \in (-n_5, n_5) \cup (n_5, \infty) \cup (-\infty, -n_5)$, as illustrated in Figure 6(a). The bounded segment $(-n_5, n_5)$ corresponds to the heteroclinic orbit shown in cyan, while the unbounded regions represent extensions of this orbit, highlighted in pink in the same figure. Assuming the initial condition $\psi(0) = 0$ and integrating the 1D form (3.1), we obtain the explicit solution

$$\psi(\zeta) = n_5 \sqrt{1 - \frac{2(n_5^2 + n_6^2)}{2n_5^2 + n_6^2 + n_6^2 \cosh\left(n_5 \sqrt{\frac{-4r}{3}(n_5^2 + n_6^2)}\,\zeta\right)}}. \tag{3.27}$$

Substituting (3.27) into (2.8) yields the corresponding phase function

$$\mu_9(\zeta) = \frac{2\varpi + 4a_1\beta - 3a_5 n_5^2}{4a_1}\zeta + \frac{3a_5\sqrt{3}}{4a_1\sqrt{-r}} \operatorname{arctanh}\left(\frac{n_5}{\sqrt{n_5^2 + n_6^2}} \tanh\left(\frac{n_5}{3}\sqrt{-3r(n_5^2 + n_6^2)}\,\zeta\right)\right). \tag{3.28}$$

Therefore, Eq (1.1) admits a novel solution of the form

$$\phi_9(\zeta) = n_5 \sqrt{1 - \frac{2(n_5^2 + n_6^2)}{2n_5^2 + n_6^2 + n_6^2 \cosh\left(n_5 \sqrt{\frac{-4r}{3}(n_5^2 + n_6^2)}\,\zeta\right)}} \exp\left[i(\alpha t - \beta x) + i\mu_9(\zeta)\right]. \tag{3.29}$$

(b) If $r > 0$, $p > 0$, $q < -2\sqrt{pq}$, and $\nu = \nu_F$, the system exhibits a composite phase orbit consisting of two homoclinic loops and a heteroclinic connection, as illustrated in blue in Figure 3(a). Under these conditions, the polynomial $\mathcal{M}$ possesses two double roots located at the saddle points F_1 and F_2, denoted by $\pm n_7$, along with two simple roots $\pm n_8$, satisfying $0 < n_7 < n_8$, as shown in Figure 6(b). Accordingly, the polynomial takes the form

$$\mathcal{M} = \frac{r}{3}(\psi^2 - n_7^2)^2(n_8^2 - \psi^2).$$

Real-valued solutions exist within the intervals $\psi \in (-n_8, -n_7) \cup (n_7, n_8) \cup (-n_7, n_7)$. The first two intervals correspond to solitary wave profiles associated with homoclinic orbits, while the central interval yields kink or anti-kink structures arising from the heteroclinic connection.

Assuming $\psi(0) = 0$ and integrating the 1D form (3.1), we obtain the solution

$$\psi(\zeta) = \pm n_7 \sqrt{1 + \frac{2(n_7^2 - n_8^2)}{n_8^2 - 2n_7^2 + n_8^2 \cosh\left(n_7 \sqrt{\frac{4r}{3}(n_8^2 - n_7^2)}\,\zeta\right)}}. \tag{3.30}$$

Substituting (3.30) into (2.8) yields the corresponding phase function

$$\mu_{10}(\zeta) = \frac{2\varpi + 4a_1\beta - 3a_5 n_7^2}{4a_1}\zeta + \frac{3\sqrt{3}a_5}{4a_1\sqrt{r}} \arctan\left(\frac{n_7}{\sqrt{n_8^2 - n_7^2}} \tanh\left(n_7\sqrt{\frac{r}{3}(n_8^2 - n_7^2)}\,\zeta\right)\right). \tag{3.31}$$

Thus, Eq (1.1) admits a new solution of the form

$$\phi_{10}(\zeta) = \pm n_7 \sqrt{1 + \frac{2(n_7^2 - n_8^2)}{n_8^2 - 2n_7^2 + n_8^2 \cosh\left(n_7 \sqrt{\frac{4r}{3}(n_8^2 - n_7^2)}\,\zeta\right)}} \exp\left[i(\alpha t - \beta x) + i\mu_{10}(\zeta)\right]. \tag{3.32}$$

Similarly, by considering $\psi \in (n_7, n_8)$ and setting $\psi(0) = n_8$, we derive another solution to Eq (1.1):

$$\phi_{11}(\zeta) = n_7 \sqrt{1 - \frac{2(n_7^2 - n_8^2)}{2n_7^2 - n_8^2 + n_8^2 \cosh\left(2n_7 \sqrt{\frac{r}{3}(n_8^2 - n_7^2)}\,\zeta\right)}} \exp\left[i(\alpha t - \beta x) + i\mu_{11}(\zeta)\right], \tag{3.33}$$

where

$$\mu_{11}(\zeta) = \frac{2\varpi + 4a_1\beta - 3a_5 n_7^2}{4a_1}\zeta + \frac{3\sqrt{3}a_5}{4a_1\sqrt{r}} \arctan\left(\frac{\sqrt{n_8^2 - n_7^2}}{n_7} \tanh\left(n_7 \sqrt{\frac{r}{3}(n_8^2 - n_7^2)}\,\zeta\right)\right). \tag{3.34}$$

Remark 1. *We provide a detailed comparison between the solutions obtained in this study and those reported in the literature [21, 25–27]. The present analysis establishes the existence criteria for periodic, solitary, and kink (anti-kink) wave solutions, as summarized in Tables 2–4. Moreover, our formulation explicitly constructs these solutions by integrating the conserved quantity over the intervals of a real wave propagation domain—an aspect ignored in earlier works despite its importance. The current results differ fundamentally from those in [25–27], where the solutions were restricted to trigonometric, hyperbolic, or rational forms. In contrast, the approach in [21] is based on the real roots of a quartic polynomial, whereas our solutions depend on the six (real or complex) roots of a sixth-degree polynomial.*

4. Graphic representation

Graphical representations are essential for revealing the intricate dynamics of mathematical models, such as the generalized derivative resonant NSL equation with cubic–quintic nonlinearity. In this section, we present a visual analysis of selected solutions using both 2D and 3D plots to emphasize their structural characteristics. Furthermore, we demonstrate the construction of solutions to Eq (1.1) and examine how these solutions undergo bifurcation for different values of the parameter ν, which we designate as the bifurcation parameter.

Our analysis begins with the parameter set $a_1 = 1, a_5 = 0.2, a_4 = 2, a_2 = 0.3, \beta = 0.3, a_3 = -6.0075$, $\alpha = 5892.15$, and $\varpi = 153$. Substitution into Eq (2.10) yields the potential coefficients $p = -2$, $r = 2$, and $q = 5$. For these values, the dynamic system (2.11) possesses three equilibrium points: The origin $O = (0, 0)$ and the symmetric pair $B_{1,2} = (\pm 0.5922677261, 0)$. The corresponding bifurcation parameter is $\nu_B = -0.1825843098$, and the phase portrait for this configuration is shown in Figure 2(c). The solution's character is governed by the value of ν for these fixed values of p, q, and r. We now examine the solutions for different ranges of ν, as indicated by the bifurcation analysis.

Case 1: Periodic Solution ($\nu \in (\nu_B, 0)$)**.** For $\nu \in (-0.1825843098, 0)$, the system exhibits a family of periodic blue orbits in Figure 2(c), corresponding to the solution of (3.14). The 2D and 3D representations of $|\phi_4|$ in Figure 7 confirm the periodic nature of this solution.

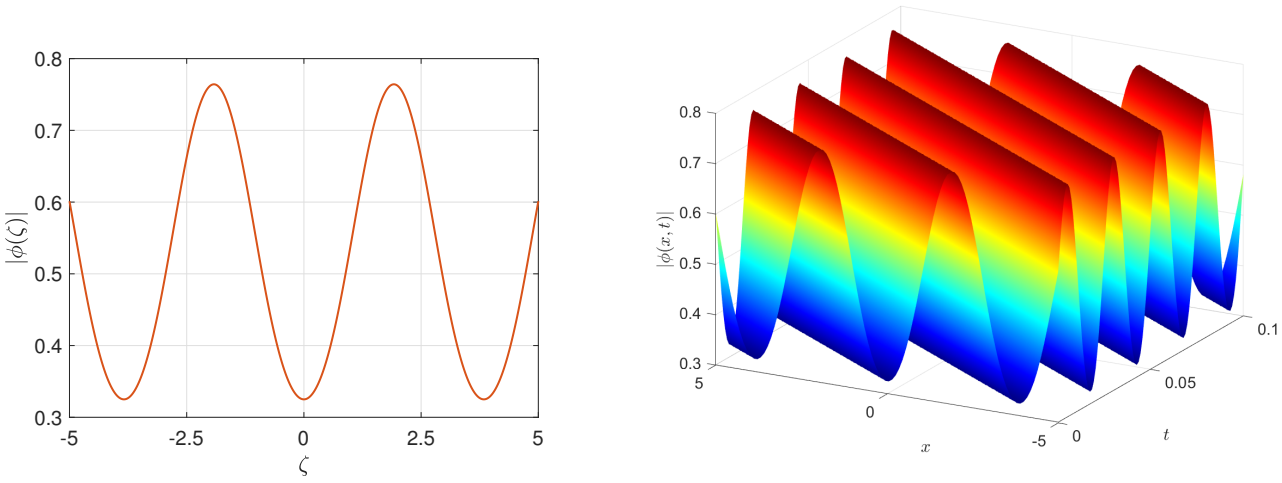

Figure 7. Graphical representation of $|\phi_4|$ given by Eq (3.14).

Case 2: Solitary Wave Solution ($\nu = 0$)**.** At $\nu = 0$, a green homoclinic orbit connects the saddle point O to itself, yielding the solitary wave solution (3.23). Figure 8 displays $|\phi_7|$ in 2D and 3D, revealing a profile that is symmetric about $\zeta = 0$.

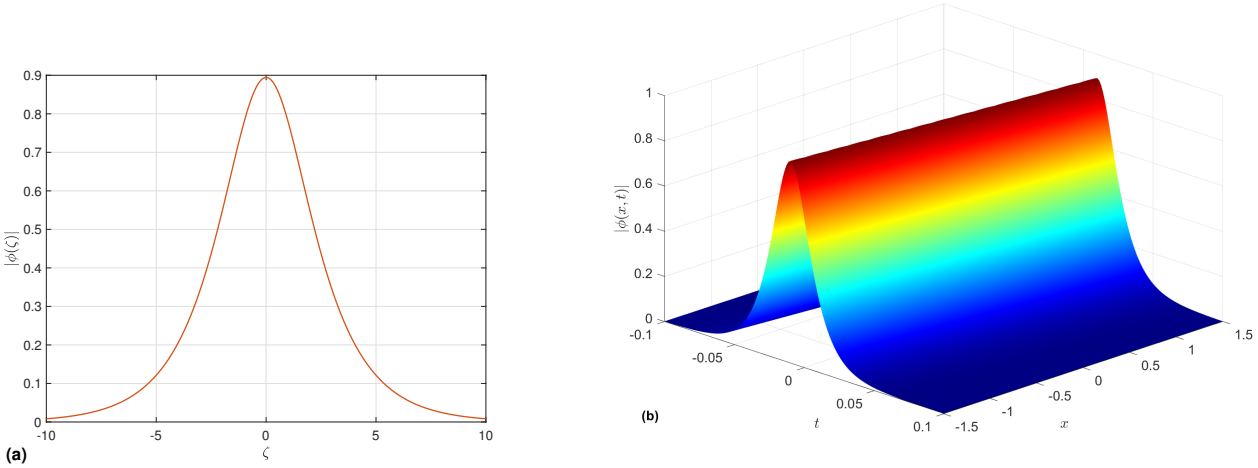

Figure 8. Graphical representation of $|\phi_7|$ given by Eq (3.23).

Case 3: Super-periodic Solution ($\nu > 0$)**.** For $\nu > 0$, the system features a family of super-periodic gold orbits (Figure 2(c)), described by the solution of (3.5) with the given p, q, and r. The 2D and 3D plots of $|\phi_1|$ in Figure 9 illustrate this super-periodic structure.

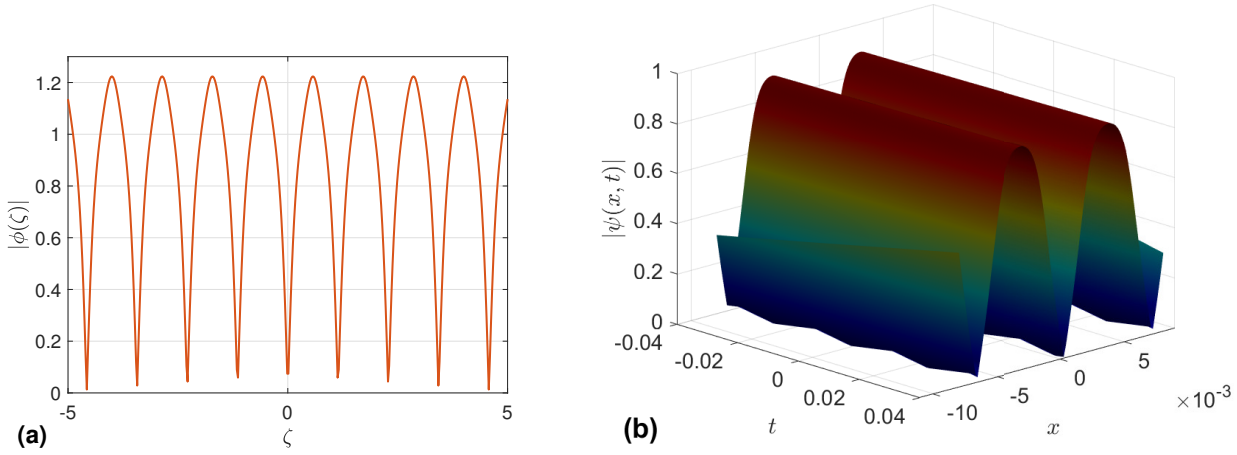

Figure 9. Graphical representation of $|\phi_1|$ given by Eq (3.5).

The phase portrait in Figure 2(c) contains no heteroclinic orbit, implying the absence of kink (or anti-kink) solutions to Eq (1.1) for the initial parameters. To obtain such a solution, we consider a new parameter set $a_1 = 1, a_5 = 0.2, a_4 = 2, a_2 = 0.3, \beta = 0.3, a_3 = 6, \alpha = 5904.15$, and $\varpi = 153$. Substitution into (2.10) now gives $p = 2$, $r = -2$, and $q = 5$. The resulting phase portrait (Figure 2) features a blue heteroclinic orbit connecting the two saddle points at $(\pm 1.688425577, 0)$. The corresponding kink solution to Eq (1.1) is given by (3.29). Figure 10 shows the 2D and 3D plots of $|\phi_9|$, which exhibits a soliton-like profile. We plot the modulus $|\phi_9|$ due to the complex functional form of the solution arising from the exponential ansatz in (2.1).

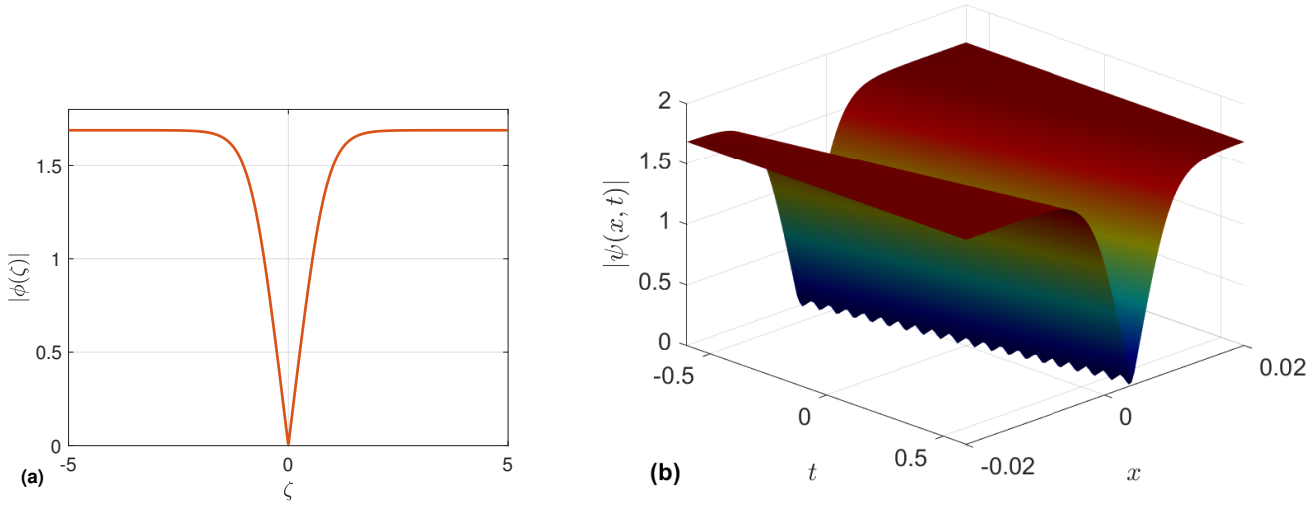

Figure 10. Graphical representation of $|\phi_9|$ given by Eq (3.29).

5. Perturbed dynamics

We analyze autoresonance in the non-autonomous system, where the oscillator synchronizes with a varying periodic excitation. The perturbed system is derived from Eq (1.1) by introducing specific forcing terms that model the influence of external forces. The perturbed version of Eq (1.1) is assumed to have the form

$$\begin{aligned} &i\frac{\partial\phi}{\partial t} + a_1\frac{\partial^2\psi}{\partial x^2} + a_2(|\phi|^2\phi) + a_3(|\phi|^4\phi) + a_4\left(\frac{\frac{\partial^2|\phi|}{\partial x^2}}{|\phi|}\right)\phi + ia_5\frac{\partial}{\partial x}\left(|\phi|^2\phi\right) \\ &- (a_1 + a_4)\ell\,\mathrm{cn}(\vartheta\zeta, \varsigma)\exp[i(\alpha t - \beta x) + i\mu(\zeta)] = 0, \end{aligned} \tag{5.1}$$

where ℓ is the strength of the perturbed force with a frequency ϑ while ς ($|\varsigma| < 1$) is the modules to the perturbed term characterized by the Jacobi-elliptic function, cn [33]. The choice of a Jacobi elliptic forcing term, $\mathrm{cn}(\zeta, \varsigma)$, is motivated by its ability to model a wide range of periodic perturbations in nonlinear optical and dispersive media. It interpolates between trigonometric and hyperbolic regimes: It simplifies to a trigonometric cosine as $\varsigma \to 0$ and to a hyperbolic secant as $\varsigma \to 1$. Repeating the steps from Section 2, the perturbed system takes the form

$$\begin{cases} \psi' = R, \\ R' = -\psi(p + q\psi^2 + r\psi^4) + \ell\,\mathrm{cn}(\theta, \varsigma), \\ \theta' = \vartheta. \end{cases} \tag{5.2}$$

We numerically investigate the dynamics of the perturbed system (5.2), with particular emphasis on how the externally imposed periodic perturbation influences its behavior.

By carefully selecting the parameters $a_1 = 1$, $a_5 = 0.2$, $a_4 = 2$, $a_2 = 0.3$, $\beta = 0.3$, $a_3 = -2.0075$, $\alpha = 798.15$, and $\varpi = -57$, and applying Eq (2.10), we obtain $p = 1$, $q = -2$, and $r = \frac{2}{3}$. For these values, the phase portrait of the unperturbed system (2.11) is illustrated in Figure 3(a) across all admissible values of ν. When the initial condition is chosen as $(\psi(0), \psi'(0)) = (0.1, 0.134)$, the corresponding value of ν is found to be 0.0139. In this case, the system exhibits a purely periodic orbit, as depicted in Figure 11(a), with its 3D representation shown in Figure 11(b). The periodic nature of the solution is further validated by the time series plots presented in Figure 11(c),(d).

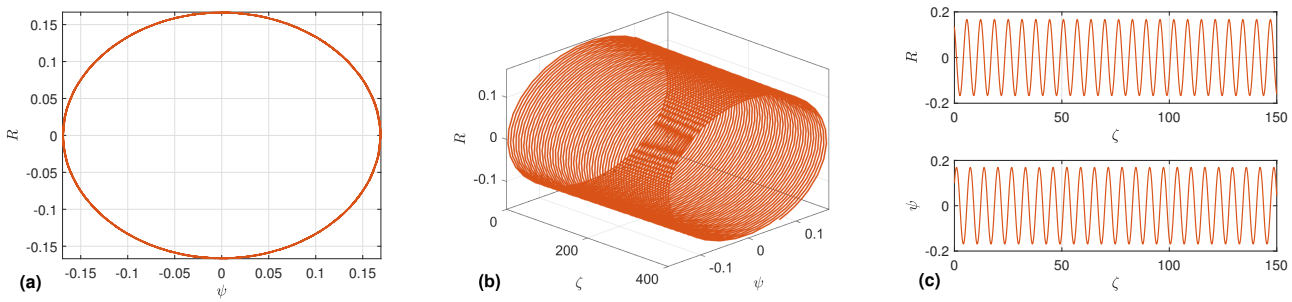

Figure 11. The dynamic behavior of the perturbed system (5.2) with $\ell = 0$, which is equivalent to the unperturbed system (2.11), for the initial condition $(\psi(0), \psi'(0)) = (0.1, 0.134)$ and parameters $p = 1$, $q = -2$, $r = 2/3$. (a) The 2D phase portrait. (b) The 3D phase portrait. (c) Time series of ψ versus ζ. (d) Time series of ψ' versus ζ.

The dynamic landscape of the unperturbed model—ranging from periodic to chaotic regimes—becomes increasingly intricate with the inclusion of the free parameters p, q, and r, in conjunction with the perturbation-related terms ℓ, ϑ, and ς. To explore these dynamics, we adopt a comprehensive strategy that combines 2D and 3D phase space visualizations, temporal evolution analysis, and sensitivity assessments with respect to the key parameters. Our investigation focuses on two illustrative cases, wherein the frequency (or amplitude) of the external excitation is varied systematically, while all other parameters are held fixed.

In the first approach, all of the system's parameters—a_i (for $i = 1, \ldots, 5$), α, β, and ϖ—are held constant, along with the initial conditions. The frequency of the external periodic excitation is fixed at $\vartheta = 1.618$, leaving the forcing amplitude ℓ as the sole varying parameter.

For a forcing amplitude of $\ell = 0.09$, the system exhibits quasi-periodic behavior, as evidenced by the 2D and 3D phase portraits and time series in Figure 12(a)–(c). This quasi-periodic regime persists when ℓ is increased to 0.12, as shown in Figure 12(d)–(f). Such behavior arises in the perturbed system (5.2) due to the presence of incommensurate frequencies.

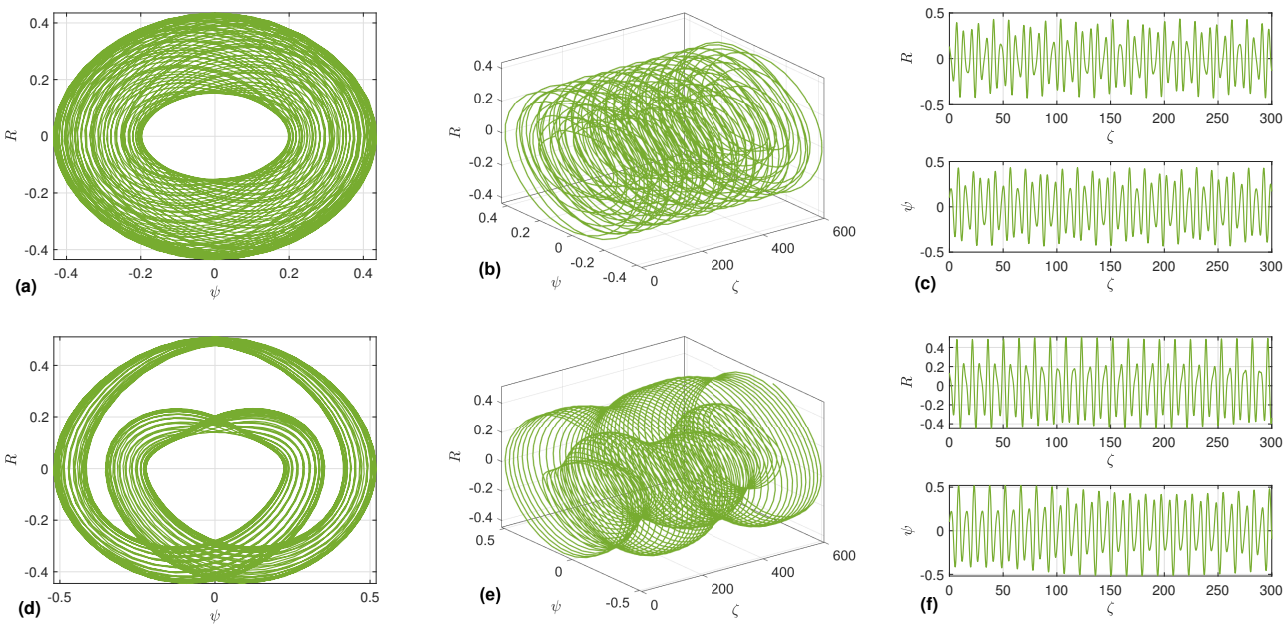

Figure 12. The dynamic behavior of the unperturbed system (2.11) with the initial conditions $(\psi(0), \psi'(0)) = (0.1, 0.134)$ and the parameters $p = 1$, $q = -2$, and $r = 2/3$. The sub-figures illustrate the system's response for two different values of the parameter ℓ: (a) 2D phase portrait for $\ell = 0.09$; (b) 3D phase portrait for $\ell = 0.09$; (c) Time series of ψ and ψ' versus ζ for $\ell = 0.09$; (d) 2D phase portrait for $\ell = 0.12$; (e) 3D phase portrait for $\ell = 0.12$; (f) Time series of ψ and ψ' versus ζ for $\ell = 0.12$.

As the forcing amplitude is further increased to $\ell = 0.2$, the system transitions to chaos, illustrated by the time series and phase portraits in Figure 13(a)–(c). This chaotic response is confirmed at $\ell = 0.4$, as displayed in Figure 13(d)–(f). To quantitatively verify the chaotic dynamics for this parameter set,

we compute the full spectrum of Lyapunov exponents as follows:

$$\varkappa_1 = 0.183505, \quad \varkappa_2 = -0.122664, \quad \varkappa_3 = 0.00. \tag{5.3}$$

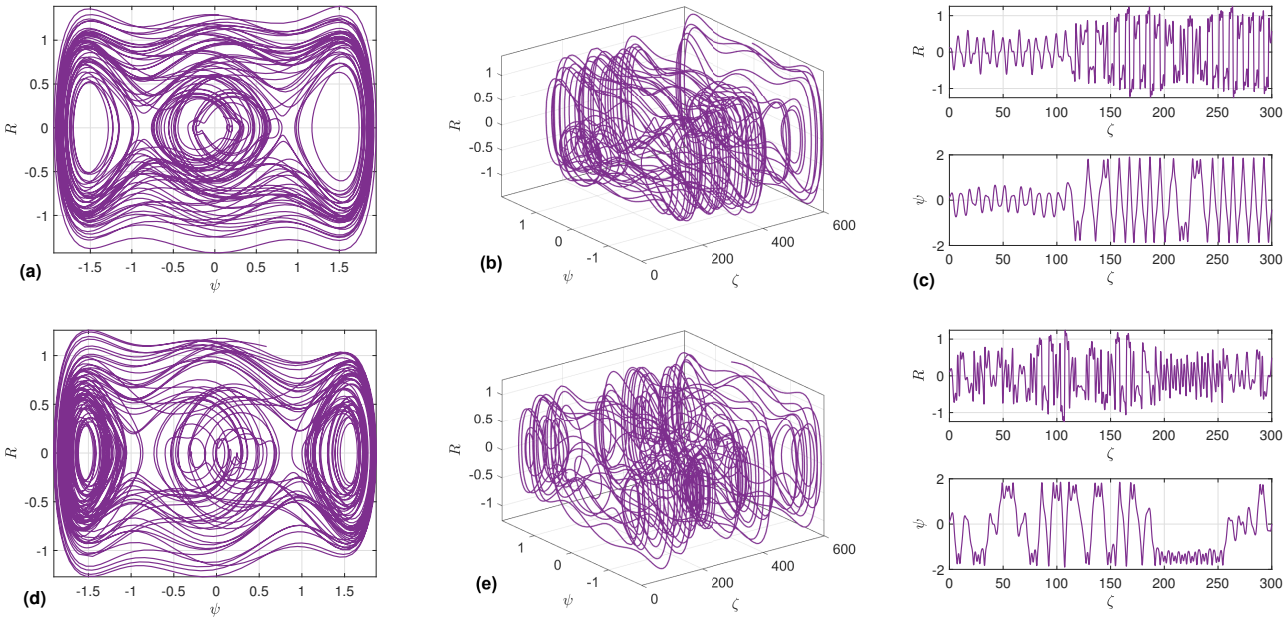

Figure 13. The dynamic behavior of the unperturbed system (2.11) with the initial conditions $(\psi(0), \psi'(0)) = (0.1, 0.134)$ and the parameters $p = 1$, $q = -2$, and $r = 2/3$. The subfigures illustrate the system's response for two different values of the parameter ℓ: (a) 2D phase portrait for $\ell = 0.2$; (b) 3D phase portrait for $\ell = 0.2$; (c) Time series of ψ and ψ' versus ζ for $\ell = 0.2$; (d) 2D phase portrait for $\ell = 0.4$; (e) 3D phase portrait for $\ell = 0.4$; (f) Time series of ψ and ψ' versus ζ for $\ell = 0.4$.

The presence of a positive exponent ($\varkappa_1 > 0$) definitively confirms the chaotic dynamics. The temporal evolution of these exponents, shown in Figure 14, demonstrates their convergence, with detailed numerical values provided in Table 5.

Further evidence of chaos is provided by the Poincaré surface of section for the same parameters, shown in Figure 15. The irregular, scattered distribution of points on this surface is a clear signature of chaotic motion, corroborating the conclusion drawn from the Lyapunov exponent analysis.

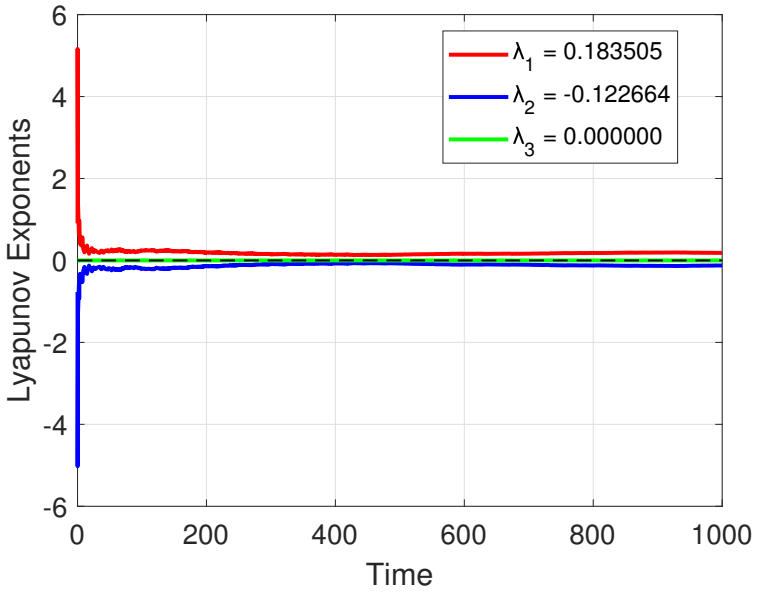

Figure 14. Convergence of Lyapunov exponents.

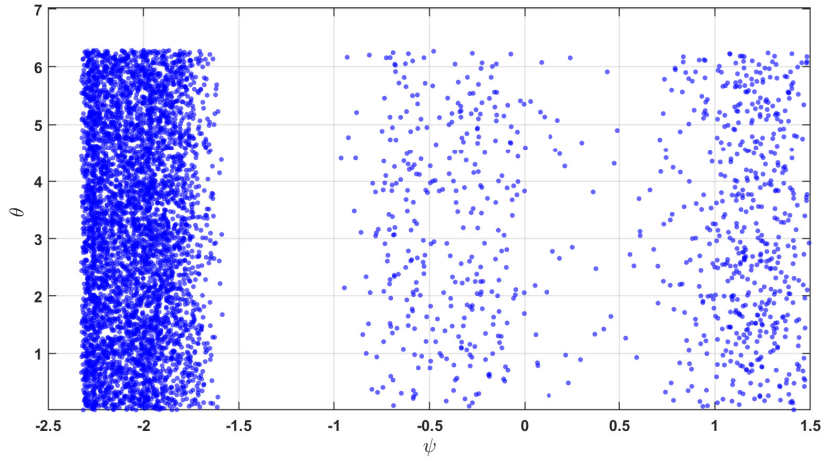

Figure 15. Poincaré section constructed with the conditions $R = 0$ and $R' > 0$. The total number of points plotted in the section is 5681.

Table 5. Lyapunov exponents' iterations.

Time	$\varkappa_1$	$\varkappa_2$	$\varkappa_3$	$\varkappa_1$	$\varkappa_2$	$\varkappa_3$	
100	0.241449	−0.200071	0.00	600	0.164939	−0.101832	0.00
200	0.194107	−0.141193	0.00	700	0.164504	−0.104311	0.00
300	0.149611	−0.087749	0.00	800	0.181640	−0.121785	0.00
400	0.137142	−0.070991	0.00	900	0.193892	−0.133704	0.00
500	0.142088	−0.074562	0.00	1000	0.183505	−0.122664	0.00

We investigate the sensitivity analysis for the perturbed system (5.2) with different initial conditions which are slightly different, as shown by Figure 16. Figure 16 illustrates the pronounced sensitivity of the perturbed GD-RNLS system to its initial conditions under strong periodic forcing ($\ell = 0.4$). Two orbits that begin almost indistinguishably close separate entirely after only a short transient interval, offering clear qualitative evidence of deterministic chaos. This observation is consistent with the quantitative indicators identified earlier: a positive largest Lyapunov exponent ($\varkappa_1 > 0$), an irregular Poincaré section, and an aperiodic time series. Collectively, these features demonstrate that the periodically driven GD-RNLS system can transition into chaotic dynamics, characterized by long-term unpredictability and the exponential divergence of nearby trajectories in phase space.

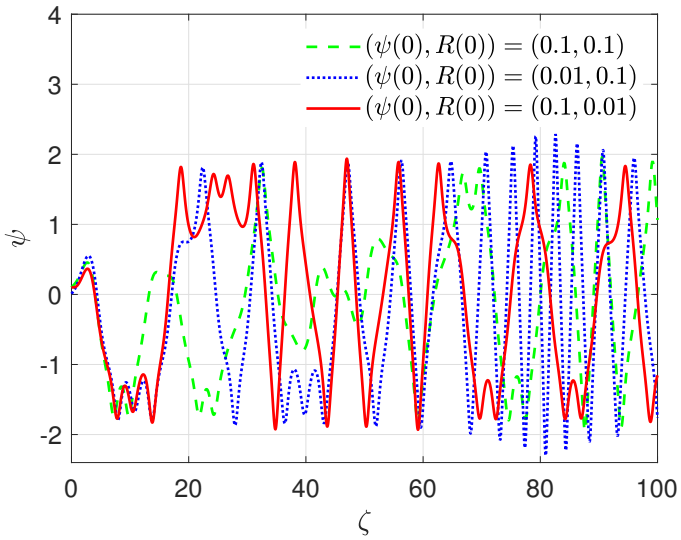

Figure 16. Sensitivity analysis of the model (5.2) with $p = 1, q = -2, r = 2/3$, and $\ell = 0.4$ with different initial conditions.

6. Conclusions

This work presents a comprehensive nonlinear analysis of the GD-RNLS, a core model for describing wave dynamics in nonlinear dispersive media with broad applications in quantum mechanics, nonlinear optics, and plasma physics. A convenient transformation is applied to the GD-RNLS, converting it into a 2D dynamic system that is equivalent to a 1D Hamiltonian system. Using Hamiltonian mechanics through the Lagrange theorem, we find the equilibrium points and classify their nature. Subsequently, the phase portraits are depicted. These portraits are described comprehensively, and we illustrate how the phase plane orbits degenerate as the bifurcation parameter varies.

Furthermore, we show that the problem of finding solutions to the GD-RNLS is equivalent to the problem of particle motion in a Hamiltonian framework. This equivalence offers several advantages. For instance, it relates the regimes of real wave propagation to the intervals of possible motion in corresponding dynamic system.Let us clarify this point briefly. For the particle motion, the conserved quantity (2.30) can be written as $\frac{1}{2}\psi'^2 = \frac{1}{2}\mathcal{M}$. Since the kinetic energy is always non-negative the real motion of the particle occurs in the region $\{\psi \in \mathbb{R} : \mathcal{M} > 0\}$, where the case $\mathcal{M} = 0$ is excluded because it corresponds to constant (and thus trivial) solutions. Thus, the intervals of real motion for the particle is also the intervals of real wave propagation. Ultimately, the bifurcation analysis provides a powerful approach for finding and characterizing solutions.

(a) This framework allows the classification of solution types prior to their construction by establishing a correspondence between solutions and phase orbits. Specifically, periodic, super-periodic, solitary, and kink (or anti-kink) wave solutions are associated with periodic, super-periodic, homoclinic, and heteroclinic orbits, respectively.

(b) This approach also permits the construction of real wave solutions by integrating the conserved quantity over the intervals of real wave propagation. These regions are indicated in cyan in Figures 4–6. The pink regions represent unbounded solutions, which are physically inadmissible. The remaining regions correspond to complex-valued solutions, which violate the hypothesis that ψ is a real-valued function.

(c) For the same parameter values p, q, r, and ν, there may be several distinct intervals supporting real wave solutions, and the corresponding profiles can differ substantially from both mathematical and physical perspectives. For example, if $p > 0$, $r > 0$, $q < -2\sqrt{pq}$, and $\nu = \nu_F$, then three admissible intervals arise, namely $\psi \in (-n_8, -n_7) \cup (-n_7, n_7) \cup (n_7, n_8)$. The outer intervals $(-n_8, -n_7)$ and (n_7, n_8) give rise to solitary wave solutions associated with homoclinic orbits, whereas the middle interval $(-n_7, n_7)$ leads to kink or antikink profiles generated by a heteroclinic connection. Thus, the structure of these real-solution intervals plays a crucial role and cannot be disregarded..

On the other hand, this approach has certain disadvantages, particularly when the dimension of the Hamiltonian system increases. For a system with a dimension greater than one, the integrability of the Hamiltonian must first be investigated. This is followed by the challenging task of constructing a sufficient number of first integrals—a number equal to the system's dimension. To our knowledge, our own work is one of the few that addresses this challenge for higher-dimensional Hamiltonian systems in this context (see, e.g., [34]).

Finally, we study a perturbed version of Eq (1.1), introducing an external periodic forcing term characterized by a Jacobi elliptic function. We numerically investigate the influence of this perturbation on the system's behavior.

First, we select parameters for the GD-RNLS equation and the assumed solution that guarantee periodic behavior in the unperturbed system (i.e., when the strength of the external forcing is zero). This is confirmed through bifurcation analysis, as well as 2D/3D phase portraits and time series.

While keeping all other parameters unchanged, we gradually increase the strength of the periodic force. This leads to the emergence of quasi-periodic behavior, which is also confirmed by 2D/3D phase portraits and time series.

With a further increase in the forcing frequency, chaotic behavior emerges, as shown by the corresponding 2D/3D portraits and time series. This chaotic state is further verified by calculating the Lyapunov exponents and the Poincaré surface of section, both of which demonstrate the irregularity of the system's dynamics.

Author contributions

Adel Elmandouh: writing the original draft, review and editing, formal analysis, software, validation, conceptualization, data curation; methodology, data duration. The author has read and approved the final version of the manuscript for publication.

Use of Generative-AI tools declaration

The author declares that he has not used artificial intelligence (AI) tools in the creation of this article.

Data availability

The data underlying the results presented in the study are available from the author upon request.

Funding

This work was supported by the Deanship of Scientific Research, Vice Presidency for Graduate Studies and Scientific Research, King Faisal University, Saudi Arabia [Grant No. KFU254233].

Acknowledgments

The author acknowledges the Deanship of Scientific Research at King Faisal University for the financial support.

Conflict of interest

The author declares no conflict of interest.

Appendix

Linear stability analysis of the 1D Hamiltonian system

Consider the Hamiltonian

$$\mathcal{H} = \frac{1}{2}R^2 + V(\psi). \tag{A.1}$$

The corresponding canonical Hamilton equations are

$$\psi' = R, \tag{A.2a}$$

$$R' = -\frac{\partial \mathcal{H}}{\partial \psi} = -\frac{dV}{d\psi}. \tag{A.2b}$$

The equilibrium points of the system (A.2) satisfy $\psi' = 0$ and $R' = 0$. Thus, they occur at $(\psi_e, 0)$, where ψ_e solves

$$\frac{dV}{d\psi}(\psi_e) = 0. \tag{A.3}$$

To determine the nature of the equilibrium $(\psi_e, 0)$, we perform a linear stability analysis by linearizing the system (A.2) around this point. When we introduce the small perturbations $z_1 = \psi - \psi_e$ and $z_2 = R$, the linearized system becomes

$$\begin{pmatrix} z_1' \\ z_2' \end{pmatrix} = \begin{pmatrix} 0 & 1 \\ -\frac{d^2V}{d\psi^2}(\psi_e) & 0 \end{pmatrix} \begin{pmatrix} z_1 \\ z_2 \end{pmatrix}. \tag{A.4}$$

The eigenvalues of the Jacobian matrix are

$$\lambda_{1,2} = \pm \sqrt{-\frac{d^2V}{d\psi^2}(\psi_e)}. \tag{A.5}$$

Thus, the equilibrium $(\psi_e, 0)$ is [32]:

- A *center* if $\frac{d^2V}{d\psi^2}(\psi_e) > 0$ (local minimum of V);
- A *saddle* if $\frac{d^2V}{d\psi^2}(\psi_e) < 0$ (local maximum of V);
- A *cusp* if $\frac{d^2V}{d\psi^2}(\psi_e) = 0$.

References

1. Y. Zhu, J. Yang, J. Li, L. Hu, Q. Zhou, Interaction properties of double-hump solitons in the dispersion decreasing fiber, *Nonlinear Dyn.*, **109** (2022), 1047–1052. https://doi.org/10.1007/s11071-022-07491-7
2. J. Yang, Y. Zhu, W. Qin, S. H. Wang, C. Q. Dai, J. T. Li, Higher-dimensional soliton structures of a variable-coefficient Gross–Pitaevskii equation with partially nonlocal nonlinearity under a harmonic potential, *Nonlinear Dyn.*, **108** (2022), 2551–2562. https://doi.org/10.1007/s11071-022-07337-2

3. M. M. Roshid, M. M. Rahman, H. Or-Roshid, Effect of the nonlinear dispersive coefficient on time-dependent variable coefficient soliton solutions of the Kolmogorov–Petrovsky–Piskunov model arising in biological and chemical science, *Heliyon*, **10** (2024), e31294. https://doi.org/10.1016/j.heliyon.2024.e31294
4. S. Duran, An investigation of the physical dynamics of a traveling wave solution called a bright soliton, *Phys. Scr.*, **96** (2021), 125251. https://doi.org/10.1088/1402-4896/ac37a1
5. K. J. Wang, S. Li, K. H. Yan, Resonant multiple wave, multi-lump wave and complex N-soliton solutions to the (3+1)-dimensional Jimbo–Miwa equation, *Mod. Phys. Lett. B*, **40** (2026), 265000. https://doi.org/10.1142/S0217984926500016
6. Y. S. Özkan, E. Yaşar, Breather-type and multi-wave solutions for the (2+1)-dimensional nonlocal Gardner equation, *Appl. Math. Comput.*, **390** (2021), 125663. https://doi.org/10.1016/j.amc.2020.125663
7. Y. S. Özkan, A. R. Seadawy, E. Yaşar, Multi-wave, breather and interaction solutions to the (3+1)-dimensional Vakhnenko–Parkes equation arising from the propagation of high-frequency waves in a relaxing medium, *J. Taibah Univ. Sci.*, **15** (2021), 666–678. https://doi.org/10.1080/16583655.2021.1999053
8. Y. H. Liang, K. J. Wang, Dynamics of the new exact wave solutions to the local fractional Vakhnenko–Parkes equation, *Fractals*, **34** (2025), 2550102. https://doi.org/10.1142/S0218348X25501026
9. M. Elbrolosy, A. Elmandouh, Painlevé analysis, Lie symmetry and bifurcation for the dynamical model of radial dislocations in microtubules, *Nonlinear Dyn.*, **113** (2025), 13699–13714. https://doi.org/10.1007/s11071-025-11084-5
10. X. Z. Zhang, I. Siddique, K. B. Mehdi, A. A. Elmandouh, M. Inc, Novel exact solutions, bifurcation of nonlinear and supernonlinear traveling waves for M-fractional generalized reaction Duffing model and the density dependent M-fractional diffusion reaction equation, *Results Phys.*, **37** (2022), 105485. https://doi.org/10.1016/j.rinp.2022.105485
11. A. Elmandouh, M. Al Nuwairan, M. M. El-Dessoky, Nonlinear dynamical analysis and new solutions of the space-fractional stochastic Davey–Stewartson equations for nonlinear water waves, *Mathematics*, **13** (2025), 692. https://doi.org/10.3390/math13050692
12. H. Wang, X. Wang, Bifurcations of traveling wave solutions for the mixed Korteweg-de Vries equation, *AIMS Math.*, **9** (2024), 1652–1663. https://doi.org/10.3934/math.2024081
13. Z. Li, S. Zhao, Bifurcation, chaotic behavior and solitary wave solutions for the Akbota equation, *AIMS Math.*, **9** (2024), 22590–22601. https://doi.org/10.3934/math.20241100
14. Q. Zhang, A. Ke, Bifurcations and exact solutions of generalized nonlinear Schrödinger equation, *AIMS Math.*, **10** (2025), 5158–5172. https://doi.org/10.3934/math.2025237
15. K. Farooq, A. R. Abdullah, E. Hussain, M. A. S. Murad, Chaos, Lyapunov exponent, and sensitivity demonstration of the coupled nonlinear integrable model with soliton solutions, *AIMS Math.*, **10** (2025), 22929–22957. https://doi.org/10.3934/math.20251019
16. N. A. Kudryashov, Almost general solution of the reduced higher-order nonlinear Schrödinger equation, *Optik*, **227** (2021), 166347. https://doi.org/10.1016/j.ijleo.2021.166347

17. M. Gürses, A. Pekcan, Nonlocal nonlinear Schrödinger equations and their soliton solutions, *J. Math. Phys.*, **59** (2018), 051501. https://doi.org/10.1063/1.4997835

18. A. M. Wazwaz, M. Mehanna, Bright and dark optical solitons for a new (3+1)-dimensional nonlinear Schrödinger equation, *Optik*, **241** (2021), 166985. https://doi.org/10.1016/j.ijleo.2021.166985

19. H. Triki, A. Biswas, S. P. Moshokoa, M. Belic, Optical solitons and conservation laws with quadratic-cubic nonlinearity, *Optik*, **128** (2017), 63–70, https://doi.org/10.1016/j.ijleo.2016.10.010

20. Q. Zhou, L. Liu, Y. X. Liu, H. Yu, P. Yao, C. Wei, et al., Exact optical solitons in metamaterials with cubic–quintic nonlinearity and third-order dispersion, *Nonlinear Dyn.*, **80** (2015), 1365–1371. https://doi.org/10.1007/s11071-015-1948-x

21. A. Das, B. Karmakar, A. Biswas, Y. Yıldırım, A. A. Alghamdi, Chirped periodic waves and solitary waves for a generalized derivative resonant nonlinear Schrödinger equation with cubic–quintic nonlinearity, *Nonlinear Dyn.*, **111** (2023), 15347–15371. https://doi.org/10.1007/s11071-023-08640-2

22. N. Karjanto, Modeling wave packet dynamics and exploring applications: a comprehensive guide to the nonlinear Schrödinger equation, *Mathematics*, **12** (2024), 744. https://doi.org/10.3390/math12050744

23. M. M. A. Khater, Dynamics of nonlinear time fractional equations in shallow water waves, *Int. J. Theor. Phys.*, **63** (2024), 1–12. https://doi.org/10.1007/s10773-024-05634-7

24. T. Christopoulos, O. Tsilipakos, E. E. Kriezis, Temporal coupled-mode theory in nonlinear resonant photonics: from basic principles to contemporary systems with 2D materials, dispersion, loss, and gain, *J. Appl. Phys.*, **136** (2024), 011101. https://doi.org/10.1063/5.0190631

25. A. Das, S. Jash, S. Paul, Y. A. Mondal, A. Das, Optical chirped soliton structures in generalized derivative resonant nonlinear Schrödinger equation and modulational stability analysis, *Optik*, **226** (2021), 165701. https://doi.org/10.1016/j.ijleo.2020.165701

26. S. Behera, Dynamical solutions and quadratic resonance of nonlinear perturbed Schrödinger equation, *Front. Appl. Math. Stat.*, **8** (2023), 1086766. https://doi.org/10.3389/fams.2022.1086766

27. B. Ghanbari, M. Inc, A new generalized exponential rational function method to find exact special solutions for the resonance nonlinear Schrödinger equation, *Eur. Phys. J. Plus*, **133** (2018), 142. https://doi.org/10.1140/epjp/i2018-11984-1

28. K. S. Al-Ghafri, Different physical structures of solutions for a generalized resonant dispersive nonlinear Schrödinger equation with power law nonlinearity, *J. Appl. Math.*, **2019** (2019), 6143102. https://doi.org/10.1155/2019/6143102

29. V. V. Nemytskii, *Qualitative theory of differential equations*, Princeton University Press, 2015.

30. H. Goldstein, *Classical mechanics*, USA: Addison-Wesley, 1980.

31. H. Goldstein, *Classical mechanics*, Addison-Wesley Series in Physics, Boston, MA, USA: Addison-Wesley, 1980.

32. F. Gantmacher, *Lectures in analytical mechanics*, MIR Publishers, Moscow (translated from the Russian), 1970.

33. P. F. Byrd, M. D. Friedman, *Handbook of elliptic integrals for engineers and scientists*, Springer-Verlag, New York-Heidelberg, 1971. https://doi.org/10.1007/978-3-642-65138-0

34. M. Alharbi, A. Elmandouh, M. Elbrolosy, New soliton, kink and periodic solutions for fractional space–time coupled Schrödinger equation, *Alex. Eng. J.*, **114** (2025), 123–135. https://doi.org/10.1016/j.aej.2024.11.058

AIMS Press